CD300e is a driver of the immunosuppressive tumor microenvironment and colorectal cancer progression via macrophage reprogramming

Running title: CD300e Drives TAMs in CRC

Annica Barizza[1†], Stefania Vassallo[1†], Laura Masatti[1], Mattia Laffranchi[2], Sofia Giacometti[1], Silvia Lonardi[3], Mattia Bugatti[3], Sara Coletta[1], Simone Pizzini[1], William Vermi[3], Matteo Fassan[4,5], Gaya Spolverato[6,7], Silvano Sozzani[2], Enrica Calura[1], Gaia Codolo[1*]

[1] Department of Biology, University of Padua, Padua, Italy.

[2] Department of Molecular Medicine, Laboratory affiliated with Istituto Pasteur Italia - Fondazione Cenci Bolognetti, Sapienza University of Rome, Rome, Italy.

[3] Section of Pathology, Department of Molecular and Translational Medicine, University of Brescia, 25123 Brescia, Italy.

[4] Department of Medicine (DIMED), Surgical Pathology Unit, University of Padua, Padua, Italy.

[5] Veneto Institute of Oncology, IOV-IRCCS, Padua, Italy.

[6] General Surgery 3, University Hospital of Padua, Padua, Italy

[7]Department of Surgical, Oncological and Gastroenterological Sciences (DiSCOG), University of Padua, Padua, Italy.

*Corresponding author, email address: gaia.codolo@unipd.it

† These authors contributed equally to this work

Acknowledgment

This work was supported by AIRC MFAG 23192 (to G.C.) and by AIRC IG 29244 (to S.S.)

We thank Prof. Kuo from Stanford Junior University, Redwood City, CA, USA, for kindly providing Rspo-1 cells and Prof. den Hertog from Hubrecht Institute, Utrecht, The Netherlands, for kindly providing Noggin- and WNT-producing cells. We thank Prof. Bronte from the Veneto Institute of Oncology, Padua, Italy, and Prof. Marigo from the Department of Surgical, Oncological and Gastroenterological Sciences (DiSCOG), University of Padua, Padua, Italy, for kindly providing the MC38 cell line.

We thank Javier Martin Gonzalez and Rafael Oliveira Brandão from the Transgenic Core Facility of the University of Copenhagen for the generation of the CD300e KO mouse.

Abstract

Colorectal cancer (CRC) progression is shaped by the tumor microenvironment, particularly tumor-associated macrophages (TAMs), which often adopt immunosuppressive functions. CD300e, a myeloid receptor involved in immune regulation, has an uncharacterized role in CRC. Here, we show that CD300e is selectively upregulated in tumor-infiltrating monocytes and macrophages, driving a suppressive phenotype marked by impaired antigen presentation. In vitro cocultures of patient-derived tumor organoids and human monocytes revealed that tumor-derived signals induce CD300e expression and promote a protumorigenic macrophage profile. Using CD300e knockout mice in AOM/DSS and MC38 CRC models, we found that CD300e loss reduced tumor burden, enhanced MHC expression on TAMs, and improved T-cell responses. Transcriptomic and functional analyses demonstrated that CD300e-deficient macrophages exhibit increased phagocytosis, upregulated antigen presentation, and greater support for T-cell proliferation and cytotoxicity. Adoptive transfer confirmed that macrophage-intrinsic CD300e expression is sufficient to suppress T-cell function and promote tumor growth. Our findings identify CD300e as a critical regulator of macrophage-mediated immune suppression in CRC and a potential target for reprogramming TAMs to enhance immunotherapy.

Keywords

Tumor, CD300e, tumor-infiltrating macrophages, colorectal cancer, immune suppression

66 ## Introduction

67 Colorectal cancer (CRC) is the most common malignancy of the gastrointestinal tract and the second
68 most common cause of death related to cancer[1,2]. Emerging evidence has revealed the pivotal
69 role of signals derived from the tumor microenvironment (TME) in the development and
70 progression of CRC. The TME comprises not only malignant cells but also infiltrating immune cells,
71 stromal cells, vasculature, and a milieu of secreted factors and extracellular matrix components
72 [3,4]. Within this complex ecosystem, immune cells, particularly T lymphocytes and myeloid cells,
73 play a dual role, either promoting tumor elimination or enabling immune escape and tumor growth,
74 depending on their functional orientation.

75 Recent studies have revealed a strong correlation between the immune landscape of the TME and
76 clinical outcomes in CRC patients [5,6]. The development of the Immunoscore system, which
77 quantifies cytotoxic T-cell infiltration in tumor tissue, has underscored the prognostic value of
78 immune composition in CRC, often surpassing conventional TNM staging in predicting patient
79 survival [7,8]. Despite this, many CRC patients exhibit poor responses to immune checkpoint
80 blockade therapies, suggesting the presence of dominant immunosuppressive mechanisms within
81 the TME that inhibit effective antitumor immunity.

82 Among the immune populations that support cancer growth in the TME, tumor-associated
83 macrophages (TAMs) are the most abundant [9–11]. Although macrophages have the potential to
84 mount a robust antitumor response, the phenotype of TAMs becomes progressively skewed toward
85 an immunosuppressive, tumor-promoting profile as cancer progresses [12,13]. This reprogramming
86 is driven by tumor-derived signals and results in a macrophage population that suppresses cytotoxic
87 lymphocyte function, promotes angiogenesis, remodels the extracellular matrix, and facilitates
88 metastatic dissemination [14]. For example, TAMs can inhibit the recruitment of $CD8^+$ T cells to the
89 tumor site, impair antigen presentation, engage immune checkpoints pathways, and foster the

90 expansion of regulatory T (Treg) cells [15,16]. High TAM infiltration in CRC has been consistently
91 associated with worse clinical outcomes, poor responses to immunotherapy, and tumor resistance
92 to conventional treatments [17–20].
93 Given their central role in modulating the immune contexture of tumors, TAMs have emerged as
94 promising therapeutic targets. However, clinical strategies aimed at depleting or reprogramming
95 TAMs have yielded limited efficacy, emphasizing the need to better understand the molecular
96 signals that govern TAM behaviour in the TME [21–23].
97 One emerging candidate is CD300e, an immune receptor expressed predominantly on myeloid cells,
98 including monocytes and macrophages, in both humans and mice [24,25]. Initially classified as an
99 activating receptor due to its association with pro-inflammatory signaling [26], CD300e has more
100 recently been implicated in negative regulation of immune responses. Notably, CD300e
101 engagement impairs macrophage-mediated T-cell activation by inhibiting antigen presentation,
102 thus promoting immune evasion [27,28]. Moreover, upregulation of CD300e has been linked to a
103 regenerative or immunosuppressive macrophage phenotype in various pathological contexts [29–
104 31]. Despite its expression in several tumor types, including CRC, the functional role of CD300e in
105 tumor immunity remains uncharacterized. Intriguingly, elevated CD300e expression correlates with
106 poor prognosis across multiple cancer types, positioning it as a potential immune regulatory
107 checkpoint [32,33].
108 In this study, we identify CD300e as a previously unrecognized driver of macrophage-mediated
109 immune suppression in CRC. Through analysis of patient-derived samples, we show that CD300e is
110 selectively upregulated in TAMs with a protumoral, immunosuppressive phenotype. Using patient-
111 derived organoid–monocyte co-cultures, we demonstrate that tumor-derived cues are sufficient to
112 induce CD300e expression and polarize macrophages toward a tumor-promoting state. In murine
113 CRC models, genetic ablation of CD300e reduced tumor burden, enhanced MHC expression on

TAMs, and restored T-cell-mediated antitumor responses. Our findings reveal a novel immunosuppressive pathway mediated by CD300e and suggest that therapeutic targeting of this receptor may reprogram TAMs and enhance the efficacy of immunotherapy in CRC.

136 # Materials and methods

137 **Subjects**

138 Surgical resections of tumor (CRC) and normal (NC) colonic tissue were collected from 8 CRC patients
139 who underwent curative-intent surgery (General Surgery 3, University Hospital of Padua) following
140 ethical standards, the Declaration of Helsinki, and national and international guidelines. Written
141 informed consent was obtained from the individual patients, and the Ethical Committee of Padua
142 University Hospital approved the protocol (Protocol Number: P448). The inclusion criteria for the
143 enrolled patients were as follows: patients with histologically confirmed primary adenocarcinoma
144 of the colon, patients aged >18 years, and patients who provided written informed consent. Patients
145 with a known history of hereditary colorectal cancer syndrome and patients who had undergone
146 neoadjuvant treatments were excluded. The patients' characteristics are detailed in Table 1.
147 The peripheral blood mononuclear cells utilized in this study were derived from buffy coats obtained
148 from healthy blood donors and anonymously provided by the Transfusion Centre of the University
149 Hospital of Padua because of voluntary and informed blood donation for transfusions. Written
150 informed consent for the use of the buffy coats for research purposes was obtained from blood
151 donors by the Transfusion Centre.
152 Further experimental details are available in the online supplemental materials and methods
153 section.

154 **Tumor and normal colon organoids**

155 *Generation of patient-derived organoids*

156 Patient-derived tumor colon organoids (TCOs) were generated from surgical resections of CRC
157 patients' primary tumor tissue, as previously reported by Sato et al. [34]. The tumor tissue was
158 minced into small pieces (2–4 mm) and digested in DMEM supplemented with 2% FBS, 2 mg/mL
159 collagenase II (Sigma Aldrich, St. Louis, MO, USA), 100 µg/mL DNAse I (Roche, Basel, Switzerland),

160 100 U/mL penicillin, and 100 µg/mL streptomycin for 1 h at 37°C under constant rolling. The cell
161 suspension was filtered through a 100 µm filter, washed in Advanced DMEM/F12 (Gibco, Thermo
162 Fisher Scientific, Waltham, MA, USA) supplemented with 2 mM GlutaMAX (Gibco), 1 mM HEPES
163 (Corning, Corning, NY, USA), 100 U/mL penicillin, and 100 µg/mL streptomycin, and seeded in
164 Growth Factor Reduced (GFR) Matrigel™ (Corning) (2000 cells/µL).
165 Patient-derived normal colon organoids (NCOs) were generated from colonic crypts obtained from
166 CRC patient-matched normal mucosa. Mucosal tissue was fragmented into small pieces (2–4 mm)
167 and incubated in 3 mM EDTA or 0.5 mM dithiothreitol (DTT) in PBS with 2% FBS for 40 minutes at
168 4°C under constant rolling to allow for crypt release. The crypt suspension was filtered through a
169 100 µm filter, washed with Advanced DMEM/F12 supplemented with 2 mM GlutaMAX, 1 mM
170 HEPES, 100 U/mL penicillin, and 100 µg/mL streptomycin, and seeded in GFR Matrigel™.
171 *Organoid culture*
172 Organoids were cultured in tumor or normal colon organoid medium (advanced DMEM/F12
173 supplemented with 2 mM GlutaMAX, 10 mM HEPES, 100 U/mL penicillin, 100 µg/mL streptomycin,
174 20% R-Spondin1 conditioned medium (RCM), 10% Noggin conditioned medium (NCM), 10 mM
175 nicotinamide (Sigma Aldrich), 1X B27 supplement (Gibco), 1 mM N-acetyl-L-cysteine (Cayman
176 Chemical, Ann Arbor, MI, USA), 50 ng/mL EGF (Corning), 10 µM Y-27632 (ROCK inhibitor,
177 Selleckchem, Houston, TX, USA), 500 nM A83-01 (Tocris Bioscience, Bristol, UK), 3 µM SB202190
178 (Sigma Aldrich), and 100 µg/mL primocin (InvivoGen, San Diego, CA, USA)). Fifty percent Wnt-3a-
179 conditioned medium (WCM) was added to normal colon organoid medium. Gastrin I (10 nM, Sigma
180 Aldrich) and prostaglandin E2 (10 nM, Sigma Aldrich) were added to the medium of both patient-
181 derived TCO and NCO. WCM, RCM and NCM were obtained from Wnt-3a-, R-spondin1-, and Noggin-
182 producing cell lines, respectively. Organoids were passaged 6–7 days after seeding and then once a
183 week.

184 **Monocyte purification, macrophage differentiation and polarization**

185 Human monocytes were purified from buffy coats of healthy donors as reported elsewhere [35] or
186 via a Pan Monocyte Isolation Kit (Miltenyi Biotec, Bergisch Gladbach, North Rhine-Westphalia,
187 Germany) following the manufacturer's instructions.

188 Mouse bone marrow cells were isolated to purify monocytes and differentiate into macrophages in
189 vitro. Bone marrow cells were obtained by flushing femurs and tibias with RPMI medium
190 supplemented with 10% FBS, 100 U/mL penicillin, and 100 µg/mL streptomycin. The cells were
191 filtered through a 70 µm filter, and red blood cells were lysed via BD PharmLyse Lysing Buffer
192 (Becton Dickinson, Franklin Lakes, NJ, USA). Monocytes were purified from bone marrow cells via a
193 Monocyte Isolation Kit (BM), mouse (Miltenyi Biotec).

194 To differentiate macrophages, bone marrow cells were seeded in Petri dishes in RPMI medium
195 supplemented with 10% FBS, 100 U/mL penicillin, 100 µg/mL streptomycin, and 10% conditioned
196 medium obtained from the L929 cell line, which contained macrophage–colony stimulating factor
197 (M-CSF). Macrophage differentiation was achieved 7 days after seeding.

198 **Cell lines**

199 MC38 mouse adenocarcinoma cells were cultured in DMEM supplemented with 10% FBS, 100 U/mL
200 penicillin, and 100 µg/mL streptomycin. When ~80% confluence was reached, the cells were
201 injected into the mice. L929 mouse fibroblasts were cultured in DMEM supplemented with 10% FBS,
202 100 U/mL penicillin, and 100 µg/mL streptomycin. L929 conditioned medium was used to
203 differentiate bone marrow-derived macrophages in vitro. The Wnt-3a-, R-spondin1- and Noggin-
204 producing cell lines were cultured in DMEM supplemented with 10% FBS, 100 U/mL penicillin, and
205 100 µg/mL streptomycin, according to the datasheet.

206 **Cocultures of monocytes/macrophages and organoids**

207 Human monocytes purified from buffy coats were cocultured together with either patient-derived
208 TCOs or NCOs. Three to four days after passage, the organoid culture medium was removed, and
209 2.5×10^5 monocytes resuspended in DMEM supplemented with 10% FBS, 4 mM HEPES and 50 µg/mL
210 gentamycin were added to each organoid well. After five days of coculture,
211 monocytes/macrophages were harvested and analyzed by flow cytometry and qRT–PCR; coculture
212 supernatants were collected for analysis of cytokine content.

213 **Western blot**

214 Western blotting was performed as reported elsewhere [36]. Briefly, human NC and CRC tissues
215 from surgical resections of CRC patients were lysed in RIPA buffer (50 mM Tris-HCl, pH 7.4; 150 mM
216 NaCl; NP-40, 1%; Na-deoxycholate, 0.5%; SDS, 0.1%; 2 mM EDTA; 50 mM NaF; 1 mM Na3VO4; 1 mM
217 EGTA; and 2% PMSF) with a protease inhibitor cocktail (Millipore, Burlington, MA, USA) via
218 TissueLyser II (Qiagen, Hilden, North Rhine-Westphalia, Germany) to homogenize the tissue.
219 Proteins were quantified with a BCA protein assay kit (Thermo Fisher Scientific) according to the
220 manufacturer's instructions. Thirty micrograms of total protein from each sample was separated by
221 SDS–PAGE and transferred to PVDF membranes (Millipore). The antigens were revealed via a rabbit
222 anti-vinculin antibody (1:5000, clone 42H89L44, Invitrogen, Waltham, MA, USA) and a rabbit anti-
223 human CD300e polyclonal antibody (1:1000, Sigma Aldrich), followed by an HRP-conjugated anti-
224 rabbit IgG secondary antibody (Millipore). The blots were developed with enhanced
225 chemiluminescence substrate (EuroClone, Pero, Italy), and protein bands were detected via an
226 ImageQuant LAS 4000 (GE Healthcare, Chicago, IL, USA).

227 **Mouse experimental models**

228 *Animals*

229 The mice were housed at the Department of Biology, University of Padua Animal Facility. All
230 protocols were approved by the ethical committee of the Italian Ministry of Health (Protocols

231 number 978/2020-PR, 386/2022-PR and 858/2023-PR). The mice were housed in a temperature
232 (22–24°C) and humidity-controlled (50%) colony room and maintained on a 12 h light/dark cycle
233 with standard food and freely available water and environmental enrichment.
234 CD300e total KO and CD300e conditional KO mouse models were generated on a C57BL/6J
235 background at the Transgenic Core Facility of the University of Copenhagen via the CRISPR/Cas9
236 system in mouse zygotes. Heterozygous male mice carrying a deletion encompassing exon 2 of the
237 *Cd300E* gene in all body tissues were used as founders of the new CD300e$^{-/-}$ mouse line. Similarly,
238 heterozygous male mice with LoxP site insertions flanking exon 2 were used as founders for
239 generating the new CD300e$^{fl/fl}$ mouse line, which was crossed with LysM Cre mice to generate a
240 conditional KO mouse lacking CD300e expression on myeloid cells (CD300e^{LysM}). Wild-type
241 (CD300e$^{+/+}$) C57Bl/6j mice were used as controls for CD300e$^{-/-}$ mice, and CD300e$^{fl/fl}$ mice were used
242 as controls for CD300e^{LysM}. All experiments were conducted on age- and sex-matched 8-- to 10--
243 week-old mice housed in the same animal facility.
244 *AOM/DSS-induced colorectal cancer*
245 To induce the development of colitis-associated colorectal cancer, male mice were injected
246 intraperitoneally with a single dose of 10 mg/kg azoxymethane (AOM, Sigma Aldrich). Three days
247 later, the mice received 2% dextran sodium sulfate (DSS, molecular weight: 36–50 kDa, MP
248 Biomedicals, Irvine, CA, USA) in their drinking water for 5 days, followed by 16 days of recovery in
249 regular water. This cycle of DSS treatment was repeated two more times, and the mice were
250 sacrificed 4 weeks after the last DSS administration. The clinical course of colitis was evaluated by
251 monitoring the body weight of the mice during the experiment and the presence of diarrhea and
252 blood after the DSS cycles.
253 *Subcutaneous tumor model and macrophage adoptive transfer*

254 To establish a syngeneic tumor model, a 100 µL tumor cell suspension containing 10^6 MC38 cells in
255 a mixture of phosphate-buffered saline (PBS) and GFR Matrigel™ (1:1 ratio) was subcutaneously
256 (s.c.) engrafted into the right flank of male mice.
257 For macrophage adoptive transfer, macrophages isolated from CD300e$^{+/+}$ and CD300e$^{-/-}$ mice, as
258 well as primary bone marrow-derived macrophages (BMDMs) isolated from CD300e$^{+/+}$ and CD300e^{-}
259 $^{/-}$ mice, were polarized toward a TAM profile with ng/ml mIL-4 20 and 20 ng/ml mIL-13 (Miltenyi
260 Biotec) and mixed with MC38 cells at a ratio of 1:2, and 7.5×10^5 total cells were s.c. injected into
261 CD300e$^{+/+}$ recipient mice or CD300e$^{-/-}$, as previously reported [37].
262 The tumor dimensions were measured once the tumors were palpable. Tumor growth was
263 monitored three times per week with a digital caliper, and the tumor volume was calculated via the
264 formula $0.5 \times L \times W^2$, with L and W being the length and width, respectively. The mice were
265 euthanized on the 21st day after MC38 inoculation or when the tumors reached 1.5 cm in diameter.
266 Once excised, the final volume of the tumor was accurately calculated by multiplying the length,
267 width, and height (L × W × H).
268 **FITC-dextran permeability assays**
269 The mice were starved overnight and then orally administered 600 mg/kg FITC-dextran (4 kDa,
270 Sigma–Aldrich) through gavage. After 3 h, blood was collected in EDTA-treated tubes from the
271 submandibular vein and centrifuged at 3000 rpm for 15 min to obtain plasma. A mixture of plasma
272 and PBS (1:10 ratio) in a total volume of 100 µL was transferred to a flat-bottom black 96-well plate,
273 and the fluorescence intensity of FITC-dextran (excitation: 483 nm; emission: 530 nm) was
274 measured via an Infinite 200Pro plate reader (Tecan, Männedorf, Switzerland). The plasma
275 concentration of FITC-dextran was calculated via a standard curve obtained from serial dilutions of
276 stock FITC-dextran (100 µg/ml) in mouse plasma.
277 **Flow cytometry**

278 Flow cytometry samples were acquired via an LSRFortessa X-20 Cell Analyzer (BD Biosciences,
279 Franklin Lakes, NJ, USA), and the data were analyzed via FlowJo version 10.3 (Tree Star, Ashland,
280 OR, USA).

281 *Human monocyte-derived macrophages*

282 After 5 d of coculture with NCO or TCO, human monocyte-derived macrophages were harvested
283 from culture wells with 5 mM Na-EDTA in PBS and incubated for 10 min at room temperature with
284 a human Fc block (BD Biosciences). The cells were stained with human monocyte/macrophage panel
285 antibodies as detailed in Table 2.

286 *Murine blood and bone marrow cells*

287 Peripheral blood from 8-week-old mice was collected in EDTA-treated tubes and incubated with BD
288 PharmLyse Lysing Buffer (BD Biosciences) to lyse erythrocytes. Blood cells or bone marrow cells,
289 which were isolated as previously described, were incubated for 10 minutes at 4°C with TruStain
290 FcX™ PLUS (clone S17011E, BioLegend, San Diego, CA, USA) to saturate the Fc receptors. The cells
291 were stained with mouse blood/bone marrow panel antibodies as detailed in Table 2.

292 *Colonic adenomas and subcutaneous tumors*

293 Colonic adenomas and subcutaneous tumors were isolated and cut into small pieces of 2–4 mm in
294 Petri dishes. The minced tissues were transferred into GentleMACS Tubes (Miltenyi Biotec)
295 containing DMEM with 1 mg/mL collagenase IV (Sigma–Aldrich) and 0.5 mg/mL DNase I.
296 GentleMACS Tubes were attached to a GentleMACS Octo Dissociator (Miltenyi Biotec), and the
297 tumors were maintained for 40 minutes at 37°C under continuous rotation. The resulting cell
298 suspension was filtered through a 70 µm strainer and incubated with TruStain FcX™ PLUS. To
299 characterize the tumor-infiltrating myeloid lineage, the cells were stained with mouse myeloid panel
300 antibodies as detailed in Table 2.

301 To characterize the tumor-infiltrating lymphoid lineage, the cells were stained with mouse lymphoid
302 panel antibodies as detailed in Table 2.

303 *T cells isolated from subcutaneous tumors and lymph nodes*

304 Tumor-infiltrating lymphocytes were purified from dissociated MC38-derived tumors via the
305 EasySep Mouse T-Cell Isolation Kit (STEMCELL Technologies, Vancouver, Canada) according to the
306 manufacturer's instructions. Local lymph nodes of MC38 tumor-bearing mice and mesenteric lymph
307 nodes of AOM/DSS-treated mice were collected, placed on a 70 µm filter and mechanically
308 disrupted via a syringe plunger.

309 A total of 0.5×10^6 tumor-infiltrating lymphocytes, as well as T cells isolated from local and
310 mesenteric lymph nodes, were seeded in 48-well plates precoated with purified anti-mouse CD3
311 (1:50 in PBS; clone 145-2c11; BioLegend) in RPMI supplemented with 10% FBS, 100 U/mL penicillin,
312 and 100 µg/mL streptomycin containing Ultra-LEAF-purified anti-mouse CD28 antibody (1:1000,
313 clone 37.51, BioLegend). After overnight stimulation, BD GolgiStop protein transport inhibitor
314 (containing monensin) (1:10 in RPMI, 10% FBS, 100 U/mL penicillin, 100 µg/mL streptomycin; BD
315 Biosciences) was added, and the mixture was incubated for 5 h. The cells were subsequently
316 incubated with TruStain FcX™ PLUS, and the cells were then stained with mouse T-cell panel
317 antibodies as detailed in Table 2.

318 For intracellular IFN-γ detection, the cells were fixed and permeabilized with a Cytofix/Cytoperm™
319 Fixation/Permeabilization Kit (BD Biosciences); FMO tubes were prepared as negative controls.

320 **Immunosuppressive activity assay**

321 The immunosuppressive activity of F4/80$^+$ tumor-infiltrating cells was evaluated by determining the
322 proliferation of allogenic CellTrace™-labeled splenic T cells. Briefly, T cells were stained with 0.5 µM
323 CellTrace™ Violet Cell Proliferation Kit (Invitrogen, Molecular Probes) according to the
324 manufacturer's instructions, activated by coating with 1 µg/mL anti-CD3 and 5 µg/mL soluble anti-

325 CD28 (BioLegend) mAb and cocultured in flat-bottom 96-well plates at a 1:3 ratio with F4/80^{+}
326 macrophages isolated from CD300e$^{+/+}$ and CD300e$^{-/-}$ tumors with anti-F4/80 MicroBeads UltraPure
327 following the manufacturer's instructions (Miltenyi Biotec). After four days at 37°C and 5% CO2, T-
328 cell proliferation was assessed by staining the cells with an anti-CD3 APC mAb (BioLegend) for flow
329 cytometry analysis and analyzing them with a BD™ LSRII flow cytometer (BD Biosciences). The T-cell
330 proliferation index was analyzed with FlowJo 10.3 and calculated as the total number of divisions
331 divided by the number of cells that went into division.

332 **Histology**

333 *Hematoxylin and eosin*

334 Hematoxylin and eosin (H&E) staining of liver, spleen, and colon samples was performed on
335 formalin-fixed, paraffin-embedded (FFPE) tissue sections. Slices were hydrated, stained with
336 Mayer's hematoxylin (Bio-Optica, Milan, Italy) and Eosin Y 1% aqueous solution (Bio-Optica) and
337 dehydrated in ethanol. Images were acquired with a Leica DM6 microscope (Leica Biosystems,
338 Nussloch, Germany) via LasX software.

339 *Immunohistochemistry*

340 Immunohistochemistry of matched NC and CRC tissues from CRC patients was performed in
341 collaboration with the University of Brescia. FFPE tissue sections were sequentially immunostained
342 as described previously [38]. Briefly, MHC-II (clone V1030, dilution 1:500; Biomeda, Foster City, CA,
343 USA) was revealed via Novolink Polymer (Leica Biosystems). The slides were then decoloured with
344 ethanol, and the previous antibody was stripped with a β-mercaptoethanol/SDS solution in a water
345 bath preheated at 56°C. Double immunohistochemistry using anti-CD163 (dilution 1:80, clone 10D6,
346 Thermo Fisher Scientific) and polyclonal rabbit anti-CD300e (Sigma Aldrich) was performed on the
347 same sections. The first was revealed using Mach4AP Polymer (Biocare Medical, Concord, CA, USA)
348 and Ferangi Blue as a chromogen, and the second was revealed using Novolink Polymer (Leica

349 Biosystems) followed by diaminobenzidine (DB). The two digital slides were synchronized via
350 ImageScope, and pictures of the same area were taken to highlight the same cells sequentially
351 stained for MHC-II/CD300e and CD163. The cells were quantified via optical counting via the
352 ImageScope count tool.

353 **ELISA**

354 The cytokine content in the coculture supernatants was evaluated with ELISA kits specific for human
355 IL-6 (Thermo Fisher Scientific) and IL-10 (Thermo Fisher Scientific) following the manufacturer's
356 instructions and an Infinite F200 Pro plate reader (Tecan).

357 **RNA extraction and qRT–PCR**

358 Total RNA was extracted with TRIzol reagent (Thermo Fisher Scientific) according to the
359 manufacturer's protocol. When working with human or murine colon tissues, the tissue was first
360 disrupted via TissueLyser II (Qiagen). The RNA was quantified via a NanoDrop 1000
361 spectrophotometer (NanoDrop, Wilmington, DE, USA). One microgram of total RNA was reverse
362 transcribed via a high-capacity cDNA reverse transcription kit (Applied Biosystems, Waltham, MA,
363 USA) following the manufacturer's instructions. Five nanograms of cDNA was used for qRT–PCR (15
364 ng when working with tissues), which was performed with PowerUp SYBR Green master mix
365 (Thermo Fisher Scientific). qRT–PCR was performed in a QuantStudio5 Real-Time PCR System
366 (Thermo Fisher Scientific) according to the following cycle: 95°C for 5 min, 95°C for 15 s, and 60°C
367 for 1 min for 40 cycles. The experiments were performed with at least three technical replicates.
368 For each sample, the data were normalized to the endogenous reference genes 18S and/or β-actin.
369 The sequences of the primers used are listed in Supplementary Table 1.

370 **Bulk RNA sequencing, single-cell RNA sequencing and transcriptomic analysis**

371 *RNA sequencing of monocytes*

372 For the bulk RNA sequencing (RNA-seq) experiment, RNA extracted from BM monocytes was
373 analyzed with a 2100 Bioanalyzer (Agilent Technologies, Santa Clara, CA, USA) to assess RNA quality
374 and integrity. Samples were used only if the RNA integrity number (RIN) was greater than 7. Library
375 construction and sequencing were performed by the NGS Facility at the Department of Biology,
376 University of Padua. RNA-seq libraries were constructed via a Stranded mRNA Prep Kit (Illumina, San
377 Diego, CA, USA), and sequencing was performed on a NovaSeq 6000 instrument (Illumina) via a
378 NovaSeq 6000 S4 Reagent Kit v1.5 300 cycles (Illumina). The reads from the RNA-seq data were
379 mapped and quantified with RSEM software (v1.3.1, genome sequence GRCm39, annotations from
380 Ensembl version 109.149, [39]). Transcripts with fewer than 10 counts in at least 60% of the samples
381 per class were filtered out. Differentially expressed genes (DEGs) were computed via edgeR (version
382 3.42.4, false discovery rate (FDR)<0.05; [39,40]) to compare CD300e$^{+/+}$ and CD300e$^{-/-}$ cells. Gene
383 Ontology pathway enrichment analysis of DEGs was performed with the R package clusterProfiler
384 (version 4.8.3; [41,42]). Pathways with an FDR < 0.05 were considered significant and included in
385 the discussion. Data are available in Supplementary Table 2.

386 *Public single-cell RNA sequencing dataset of human colorectal cancer*

387 The human single-cell RNA-seq (scRNA-seq) dataset was downloaded from the GEO (GSE178341)
388 and was provided by Pelka et al. [43]. Only the cells labeled as myeloid by the original authors were
389 included in the downstream analysis. Low-quality cells (gene count <=200 or >=4000) and cells with
390 >=20% mitochondrial gene expression were removed. The filtered raw count matrix was processed
391 via the Seurat package (v5.3.0, [44]); normalizeData and ScaleData functions were applied with
392 standard options. Highly variable genes (HVGs, n=2000) were obtained via the FindVariableFeatures
393 function and informed principal component analysis (PCA). Each patient cell was integrated via the
394 Harmony R package (v0.1, [45]). Harmony integration was performed with batchID as a variable,
395 and the resulting reduction was used for graph-based clustering (resolution 0.5) and uniform

396 manifold approximation and projection (UMAP). The marker genes per cluster were obtained via
397 the FindAllMarkers function (only.pos = TRUE, min.pct = 0.25, min.diff.pct = 0.2. Data are available
398 in Supplementary Table 3.
399 Pseudotime analysis utilized Monocle3 (v1.3.1, [46]) on only the identified monocyte and
400 macrophage populations. The starting point was set to the Mono_a cluster. All the analyses were
401 conducted in R (version 4.4.3, 2025-02-28 ucrt Trophy Case) via RStudio.
402 Single-cell RNA sequencing of *CD300e$^{+/+}$ and CD300e$^{-/-}$ mouse adenomas*
403 CD45^{+} cells from three CD300e$^{+/+}$ and three CD300e$^{-/-}$ mice were isolated and independently labeled
404 via single-cell labeling with a BD single-cell multiplexing kit (BD Biosciences, #633793); next, the six
405 samples were pooled prior to FACS sorting. CD11b^{+} myeloid cells were FACS-sorted into L/D^{-}CD3e^{-}
406 CD19-CD11b^{+} cells and processed via single-cell capture and cDNA synthesis with the BD Rhapsody
407 Express single-cell analysis system following the manufacturer's protocol (BD Biosciences). The
408 resulting cDNA libraries were prepared via mRNA whole-transcriptome analysis (WTA) and a sample
409 tag library preparation protocol (BD Biosciences). Libraries were sequenced on a NovaSeq 6000
410 sequencer (Illumina).
411 The raw data were aligned via the BD Rhapsody Sequence Analysis CWL pipeline v2.2.1, with
412 RhapRef_Mouse_WTA_2023-02 used as a reference genome. The h5mu to Seurat pipeline v2.2.1
413 was subsequently used for conversion (https://openpipelines.bio/). Data processing and
414 normalization were performed through the package Seurat (v5.3.0). The single-cell expression
415 matrix was filtered (700 < nFeature_RNA < 5500 percent.mt < 25%, and 1000 < nCount_RNA <
416 100000). PCA was computed via the 2000 highly variable features obtained via the
417 FindVariableFeatures function. Graph-based unsupervised clustering and UMAP were performed by
418 selecting the first top 10 PCs.

419 The marker genes for each cluster were identified via the FindMarkers function (minpct = 0.25 and
420 p value < 0.01). Cell identity was assigned on the basis of marker genes in each cluster
421 (Supplementary Table 4). FindMarkers was used to calculate differentially expressed genes (DEGs)
422 by comparing CD300e$^{+/+}$ and CD300e$^{-/-}$ cells within each cluster (Bonferroni adjusted p value < 0.05).
423 Gene set enrichment analysis (GSEA) of the mouse ortholog hallmark gene sets (MH Mouse MSigDB,
424 v2024.1. Mm) was provided with the fgsea package (Benjamini–Hochberg adjusted p value < 0.25
425 v1.34.0, [47–49]) (Supplementary Table 5). The AddModuleScore from the Seurat package was used
426 to estimate a score per cell representing the cumulative gene expression of the DEGs of the human
427 Mono_a cluster.
428 All analyses were conducted in R (version 4.5.0, 2025-04-11) via RStudio.
429 **Statistical analyses**
430 Statistical analyses were performed with GraphPad Prism 8.0 software via one-way or two-way
431 analysis of variance (ANOVA) followed by Šídák's multiple comparisons test or Tukey's test, as
432 appropriate. For two-group comparisons, two-tailed Student's t tests were employed. All the data
433 are presented as the means ± standard deviations (SDs), unless otherwise stated, and differences
434 between groups were considered statistically significant at p<0.05. *p value≤0.05; **p value≤0.01;
435 ***p value≤0.001; ****p value≤0.0001.
436

437 # Results

438 ## Colorectal cancer promotes CD300e expression in dysfunctional tumor-infiltrating
439 macrophages

440 To address the involvement of CD300e-expressing monocytes/macrophages in the colorectal cancer
441 TME, we first investigated their expression in matched tumor and normal colon mucosa (NM)
442 derived from CRC patients. Compared with matched normal tissue, tumor mucosa presented
443 significantly increased expression of CD300e (Figure 1A), in line with previous observations linking
444 CD300e to immunosuppressive macrophage programming and impaired antigen presentation [27].
445 Building on our earlier findings that TAMs in CRC downregulate MHC-II and suppress T-cell
446 proliferation in response to tumor-derived signals [38], we assessed whether CD300e expression is
447 associated with similar transcriptional alterations. In the same patient samples, tumor-infiltrating
448 macrophages showed reduced MHC-II expression, accompanied by significant downregulation of
449 CIITA and STAT1, the latter being a key transcription factor in the IFN-γ–CIITA axis (Figure 1B). These
450 data suggest that the immunosuppressive phenotype of CD300e^{+} macrophages may result, at least
451 in part, from impaired STAT1 signaling, leading to defective antigen presentation.
452 Immunohistochemical analysis revealed that the increase in CD300e expression within CRC tissue
453 reflects enhanced infiltration of CD163^{+} macrophages co-expressing CD300e. Importantly, the
454 proportion of CD300e^{+}/MHC-II^{low} macrophages was significantly elevated in tumor tissue relative to
455 matched normal mucosa (Figure 1C), further supporting a role for CD300e in fostering a suppressive
456 myeloid compartment within the CRC microenvironment.

457 To further characterize the phenotype and functional properties of CD300e^{+} myeloid cells in CRC,
458 we leveraged a publicly available scRNA-seq dataset (GSE178341) [43] from primary tumor and
459 adjacent normal samples from untreated CRC patients. Given that *CD300E* is predominantly

460 expressed by myeloid cells, we focused our analysis on this compartment, and we identified 20
461 distinct clusters organized in granulocytes, monocytes, macrophages and dendritic cells based on
462 their transcriptional profiles and the previous authors classification (Figure 1D and Supplementary
463 Table 2). A comparison of cluster distributions between normal and tumor tissues revealed
464 increased monocyte infiltration in tumor samples (Figure 1E and Supplementary Table 2). Whereas
465 monocytes and macrophages account for approximately two-thirds of the myeloid compartment in
466 normal tissues, their proportion is notably reduced in tumors, resulting in a more heterogeneous
467 myeloid composition. *CD300E* expression was enriched in several monocyte clusters (Mono_a,
468 Mono_b, Mono_C and Mono_d) and in one macrophage cluster characterized by an active
469 interferon gene signature (Macro_IFN). Although monocytes and macrophages were the most
470 abundant cell types in normal samples, *CD300E* expression was upregulated in tumor-infiltrating
471 cells compared with their normal counterparts. Among these clusters, the Mono_a cluster
472 presented significantly increased mean expression of *CD300E* in tumor tissues (Figure 1F). Given the
473 positivity for *CD300E* of tumor derived monocyte and selected macrophage clusters, and by
474 considering that the majority of tumor-infiltrating macrophages differentiate from recruited
475 circulating monocytes, we performed a pseudotime trajectory analysis restricted to monocytes and
476 macrophages, which revealed the expected progression from monocyte to macrophages
477 (Supplementary Figure 1 A, B). Notably, as shown in Supplementary Figure 1C, the expression of
478 *CD300E* decreased along the monocyte maturation trajectory and terminated approximately when
479 there was a switch from Macro_IFN to Macro_c. In summary, in CRC the *CD300E* expression is largely
480 confined to tumor-infiltrating monocytes and early monocyte-derived macrophages.

481 ## The colorectal tumor cells drives the differentiation of immunosuppressive CD300e^{+}
482 ## macrophages

483 Given that CD300e^{+} monocyte-derived macrophages in CRC tumors display an immunosuppressive
484 profile, we sought to determine whether this phenotype could be directly instructed by the tumor
485 epithelium. To this end, we established an in vitro coculture system using patient-derived tumor
486 colon organoids (TCOs) and matched normal colon organoids (NCOs), which were incubated with
487 peripheral blood monocytes (Figure 2A). After 5 days of coculture, monocytes exposed to both NCO
488 and TCO acquired a macrophage-like phenotype (Figure 2B), with TCO-exposed cells showing
489 distinct immunological features. Notably, TCO promoted strong upregulation of CD300e (Figure 2C),
490 downregulation of MHC-II and CD86, and increased expression of the anti-inflammatory markers
491 CD206 and CD163 relative to those in NCO-exposed cells (Figure 2D and Supplementary Figure 2).
492 Functionally, these cells also secreted increased levels of IL-6 and IL-10, two cytokines associated
493 with tumor-promoting inflammation (Figure 2E).
494 These findings indicate that the colorectal tumor epithelium actively reprograms monocytes toward
495 CD300e^{+} macrophages with reduced antigen-presenting capacity and an immunosuppressive
496 phenotype.

497 ## CD300e supports colitis-associated colon cancer development

498 To investigate whether CD300e regulates the monocyte/macrophage phenotype, we generated a
499 systemic *CD300E*-deficient mouse (Supplementary Figure 3A). In CD300e$^{+/+}$ tissues, *CD300e* was
500 expressed primarily in the blood, bone marrow (BM), and liver, which are enriched with
501 monocytes/macrophages, and at lower levels in the heart, muscle, lymph nodes, lungs, and spleen
502 (Supplementary Figure 3B). Efficient gene deletion was confirmed by assessing gene expression
503 across different tissues (Supplementary Figure 3C). Notably, *CD300e* deletion did not affect

504 leukocyte populations in the blood or BM in either sex (Supplementary Figure 3D and E), nor did it
505 alter the phenotype of peritoneal macrophages (Supplementary Figure 3F). Histological analysis
506 revealed no significant differences between CD300e$^{+/+}$ and CD300e$^{-/-}$ mice under homeostatic
507 conditions (Supplementary Figure 3G).
508 To gain molecular insight into CD300e function, we performed bulk RNA-seq on BM-derived
509 monocytes from CD300e$^{+/+}$ and CD300e$^{-/-}$ mice. Several genes were differentially expressed in the
510 absence of *CD300e* (Supplementary Figure 3H). Pathway analysis revealed enrichment of genes
511 involved in antigen presentation, immune receptor activity, cytokine signaling, and chemokine-
512 related processes (Supplementary Figure 3I). In particular, CD300e$^{-/-}$ monocytes presented
513 upregulation of MHC class II genes (*H2-Ab1*, *H2-Aa*, *H2-Eb1*, and *Cd74*) and
514 proinflammatory/immunostimulatory genes (*Tnfrsf1b*, *Il17ra*, *and Ccr7*), whereas
515 immunosuppressive and tumor-promoting genes such as *Ccl2* [50] and *Trem2* [51] were markedly
516 downregulated (Supplementary Figure 3J). These data suggest that CD300e shapes monocyte
517 identity by promoting a transcriptional program associated with immunosuppression and tumor
518 support, which is consistent with its regulatory role in human monocyte activation and function
519 [28].
520 To assess whether CD300e contributes functionally to colorectal cancer development, we employed
521 a colitis-associated colorectal cancer model using azoxymethane (AOM) and dextran sodium sulfate
522 (DSS) [52]. Although not statistically significant, CD300e$^{+/+}$ mice tended to have increased mortality,
523 particularly during the first DSS cycle (Figure 3A). CD300e$^{-/-}$ mice experienced significantly less
524 weight loss than their CD300e$^{+/+}$ counterparts did (Figure 3B), despite having comparable baseline
525 weights (Supplementary Figure 4A) and similar weight gains in untreated controls (Supplementary
526 Figure 4B). Colon shortening, a hallmark of DSS-induced injury, was significantly attenuated in
527 CD300e$^{-/-}$ mice (Figure 3C), accompanied by reduced intestinal permeability (Supplementary Figure

528 5A). The baseline colon length in the untreated mice was equivalent between the genotypes
529 (Supplementary Figure 4C).
530 Importantly, CD300e deficiency led to a significant reduction in tumor burden, as evidenced by
531 fewer neoplastic lesions and a smaller tumor area (Figure 3D), which was confirmed histologically
532 (Supplementary Figure 5B). Myeloid cell infiltration within adenomas was modestly reduced in
533 CD300e$^{-/-}$ mice, mainly due to a lower number of infiltrating neutrophils, which was consistent with
534 the AOM/DSS model (Supplementary Figure 5C). Although monocyte/macrophage infiltration was
535 limited overall, tumor-associated F4/80^{+} cells in CD300e$^{-/-}$ mice presented slightly increased MHC-I
536 and MHC-II expression (Supplementary Figure 5D). This prompted scRNA-seq analysis of adenoma-
537 infiltrating myeloid cells to evaluate potential shifts in their transcriptional profiles.
538 We observed lower overall myeloid infiltration in CD300e$^{-/-}$ mice, with neutrophils comprising the
539 predominant population (Supplementary Table 6). Among the nine identified clusters, two
540 represented monocytes/macrophages present at similar frequencies across genotypes, although
541 absolute numbers were greater in CD300e$^{+/+}$ mice (Figure 3E). A cross-species comparison revealed
542 that murine monocytes shared a transcriptional signature with the human Mono_a cluster
543 (Supplementary Figure 6), supporting functional conservation. Hallmark pathway analysis revealed
544 that CD300e$^{-/-}$ monocytes downregulated several inflammatory and tumor-associated pathways
545 that were previously upregulated in human tumor-infiltrating Mono_a and Macro_IFN cells (Figure
546 3F). Overall, CD300e$^{+/+}$ monocytes/macrophages expressed higher levels of genes associated with
547 immunosuppression and tumor support, including *Cd36, Spp1, Il6, Cd274, Ccl5, Ccl17, Ccl22, and*
548 *Ccl24* (Figure 4G and Supplementary Figure 5E) [53].
549 Although tumor-infiltrating T cells were present at a low frequency, their CD4^{+} and CD8^{+} proportions
550 were similar between genotypes (Supplementary Figure 5F). However, CD300e$^{-/-}$ mice presented a
551 significantly greater frequency of IFN-γ–producing CD8^{+} T cells in mesenteric lymph nodes (Figure

552 4H), indicating enhanced systemic antitumor immunity in the absence of CD300e. No differences in
553 T-cell activation were detected in untreated animals (Supplementary Figure 4D–E).
554 To confirm that the observed effects were due to myeloid-intrinsic CD300e, we generated
555 conditional knockout (cKO) mice in which CD300e deletion was restricted to the myeloid
556 compartment (indicated as CD300e^{LysM}) (Supplementary Figure 7A). These cKO mice recapitulated
557 the phenotype observed in global knockouts, showing reduced weight loss, decreased tumor
558 burden, and increased frequencies of IFN-γ–producing CD4^{+} and CD8^{+} T cells (Figure 4A–D and
559 Supplementary Figure 7B–C).

560 Lack of CD300e enhances antitumor immunity by reprogramming tumor-infiltrating 561 myeloid cells and increasing T-cell function

562 To further investigate the role of CD300e in shaping the tumor immune landscape, we employed a
563 subcutaneous CRC model by injecting the MC38 colon cancer cell line into CD300e$^{-/-}$ and CD300e$^{+/+}$
564 mice—an established model in which tumor progression is known to rely on the activity of tumor-
565 infiltrating macrophages [54]. While MC38 tumors grew progressively in CD300e$^{+/+}$ mice, their
566 growth was significantly impaired in CD300e$^{-/-}$ mice (Figure 5A, B), in line with the findings from the
567 AOM/DSS CRC model. To characterize the immune microenvironment, we performed flow
568 cytometry analysis of MC38 tumors 21 days postinjection (the gating strategy is shown in
569 Supplementary Figure 8). CD11b^{hi} myeloid cells were less abundant in CD300e$^{-/-}$ tumors because of
570 a reduction in both neutrophils (Figure 5C) and monocytes (CD11b^{+}Ly6C^{+}Ly6G^{-}) and monocyte-
571 derived macrophages (CD11b^{+}Ly6C^{lo}F4/80^{+}) (Figure 5D, F; Supplementary Figure 9). Despite their
572 lower abundance, monocytes and macrophages infiltrating CD300e$^{-/-}$ tumors presented significantly
573 higher expression levels of MHC-II and MHC-I molecules (Figure 5E, G), suggesting a greater
574 immunostimulatory profile in the absence of CD300e.

575 Given that elevated expression of antigen-presenting molecules is often associated with improved
576 T-cell activation, we next analyzed the lymphoid compartment. Compared with those from
577 CD300e+/+ control mice, tumors from CD300e$^{-/-}$ mice presented a greater proportion of both CD4^{+}
578 and CD8^{+} T cells (Figure 5H; gating strategy detailed in Figure S10). In addition, CD300e$^{-/-}$ tumors
579 contained increased frequencies of activated and effector memory T cells within both the CD4^{+} and
580 CD8^{+} subsets (Figure 5I, J), indicating enhanced T-cell activation. Functional profiling revealed a
581 significant increase in the number of IFN-γ-producing CD4^{+} and CD8^{+} tumor-infiltrating T
582 lymphocytes (TILs) in the CD300e$^{-/-}$ mice (Figure 5K). This heightened activation was accompanied
583 by greater cytotoxic potential, as CD8^{+} TILs from CD300e$^{-/-}$ tumors expressed higher levels of
584 granzyme B (GZMB) and perforin (Figure 5L).
585 These findings were corroborated in cKO; similar to those in full knockouts, CD300e cKO mice
586 presented reduced tumor growth, decreased myeloid infiltration, increased MHC expression on
587 myeloid cells, and an enhanced T-cell response characterized by elevated IFN-γ production and
588 CD8+ cytotoxic activity (Supplementary Figure 11).
589 To directly compare the functional properties of macrophages from CD300e+/+ and CD300e$^{-/-}$ mice,
590 we performed an ex vivo phagocytosis assay on F4/80^{+} tumor-infiltrating macrophages. CD300e$^{-/-}$
591 macrophages exhibited significantly greater phagocytosis capacity (Figure 6A), which is consistent
592 with the notion that TAMs adopt a less phagocytic, immunosuppressive phenotype during tumor
593 progression [55]. We next assessed their capacity to support T-cell activation by coculturing isolated
594 tumor macrophages with autologous T cells labeled with CellTrace proliferation dye. Strikingly,
595 compared with their CD300e+/+ counterparts, CD300e$^{-/-}$ macrophages elicited significantly greater
596 T-cell proliferation (Figure 6B).

597 Together, these results demonstrate that CD300e deficiency promotes the acquisition of a more
598 immunostimulatory macrophage phenotype, which in turn enhances T-cell activation, expansion,
599 and cytotoxicity in the TME.

600 CD300e expression on macrophages is sufficient to promote tumor growth and 601 suppress the antitumor T-cell response

602 To determine whether the tumor-promoting effects of CD300e are directly mediated by its
603 expression on macrophages, we performed adoptive transfer experiments using tumor-infiltrating
604 macrophages isolated from CD300e$^{-/-}$ and CD300e$^{+/+}$ mice. These macrophages were co-injected at
605 a 1:3 ratio with MC38 tumor cells into CD300e$^{+/+}$ recipient mice (Figure 7A). Notably, tumors from
606 mice that received CD300e$^{-/-}$-derived macrophages exhibited significantly slower tumor growth than
607 those from mice that received CD300e$^{+/+}$ macrophages (Figure 7B, C). Although the overall
608 infiltration of monocytes and macrophages within tumors was comparable between the groups, the
609 TIL profile recapitulated the immune phenotypes observed in CD300e$^{-/-}$ hosts. Specifically, recipient
610 mice injected with CD300e$^{-/-}$ macrophages presented increased frequencies of IFN-γ–producing T
611 cells (Figure 7D) and greater cytotoxic potential among CD8^{+} lymphocytes (Figure 7E).
612 To confirm these findings in an independent system, we repeated the coinjection experiment using
613 bone marrow-derived macrophages (BMDMs) polarized with IL-4 to mimic the TAM phenotype.
614 When CD300e$^{+/+}$ recipient mice were coinjected with MC38 cells and either CD300e^{-}/$^{-}$ or CD300e$^{-/-}$
615 BMDMs at a 1:3 ratio (Supplementary Figure 12A), mice receiving CD300e$^{-/-}$ BMDMs exhibited
616 reduced tumor growth (Supplementary Figure 12B–C). This effect was accompanied by a greater
617 proportion of macrophages expressing MHC-I and MHC-II (Supplementary Figure 13D) and
618 increased infiltration of activated T cells (Supplementary Figure 12E–F).

619 Conversely, when tumor-isolated macrophages from CD300e$^{+/+}$ or CD300e$^{-/-}$ donors were injected
620 into CD300e$^{-/-}$ recipient mice (Supplementary Figure 13A), those receiving CD300e$^{+/+}$ macrophages
621 presented enhanced tumor growth (Supplementary Figure 13 B, C), coupled with reduced
622 frequencies of IFN-γ-producing T cells and diminished CD8+ cytotoxic activity (Supplementary Figure
623 S13 D-F).
624 Taken together, these data provide direct evidence that CD300e expression on macrophages is
625 sufficient to drive tumor progression by dampening antitumor T-cell responses, highlighting its
626 central role in orchestrating an immunosuppressive TME.

627 ## Discussion

628 CD300e is a relatively understudied member of the CD300 family, originally described as an
629 activating molecule selectively expressed by cells of the myeloid lineage [25,26]. While emerging
630 evidence has implicated CD300e in modulating immune response during chronic inflammation and
631 infection [27,28], its role in cancer immunity has remained unexplored.

632 In this study, we provide compelling evidence that CD300e plays an active and previously
633 unrecognized role in CRC progression by enforcing an immunosuppressive program in TAMs and
634 limiting antitumor T-cell immunity. Specifically, we show that CD300e is selectively expressed by
635 tumor-infiltrating monocytes and monocyte-derived macrophages in human CRC, especially within
636 a subset exhibiting IFN-driven transcriptional features.

637 Interestingly, despite the enrichment of IFN-related gene signature, these CD300e^{+} macrophages
638 exhibit marked downregulation of key IFN effectors, including STAT1 and CIITA, the latter being the
639 master regulator of MHC-II transcription. This paradoxical finding is consistent with our previous
640 observations [28], and suggests dysregulated or suppressed IFNγ response within the tumor
641 microenvironment, leading to impaired antigen-presentation and contributing to local immune
642 suppression.

643 Importantly, our data position CD300e not merely as a marker of immunosuppressive TAMs, but as
644 a functional regulator that acts upstream of the transcriptional downregulation of the STAT1–CIITA
645 axis. This mechanistic link provides a functional explanation for earlier observations in CRC [38],
646 where MHC-II^{low}/CD206^{high} TAMs failed to support effective T-cell activation.

647 Building on prior findings that CD300e engagement can suppress MHC-II expression and
648 macrophage-mediated T-cell proliferation [27], our study now offers in vivo validation of this
649 immunoregulatory pathway in the context of cancer. By identifying CD300e as a central modulator

650 of TAM dysfunction, we add a new layer of insight into the molecular mechanisms by which the
651 tumor microenvironment subverts innate immune cells to escape immune surveillance.
652 Using a coculture system of patient-derived tumor colon organoids and primary human monocytes,
653 we further demonstrated that the tumor epithelium can directly induce CD300e expression and
654 reprogram macrophages toward an immunosuppressive phenotype. These tumor-educated
655 macrophages exhibited hallmark features of immune regulation, including downregulation of MHC-
656 II and CD86, upregulation of CD206 and CD163, and increased secretion of IL-6 and IL-10. These data
657 suggest that tumor-derived cues are sufficient to drive CD300e expression and promote the
658 emergence of an immunoregulatory TAM phenotype, capable of dampening antitumor immunity.
659 In vivo, the functional relevance of CD300e was confirmed in two complementary models of CRC:
660 the AOM/DSS-induced colitis-associated cancer model and the MC38 subcutaneous tumor model.
661 Genetic ablation of CD300e in these settings resulted in a marked reduction of tumor burden,
662 preserved intestinal barrier function, and enhanced antitumor immunity both systemically and
663 within the tumor microenvironment. CD300e-deficient mice showed decreased infiltration of
664 protumor myeloid cells, increased expression of MHC-I and MHC-II molecules both on monocytes
665 and monocyte-derived macrophages, and robust activation of $CD4^+$ and $CD8^+$ T cells. T cells included
666 an increased frequency of IFN-γ-producing and cytotoxic T lymphocytes.
667 Functional analyses further revealed that CD300e-deficient tumor-infiltrating macrophages had
668 increased phagocytic capacity and better promoted T-cell proliferation ex vivo, indicating enhanced
669 macrophage effector functions and antigen-presenting capability. These features are hallmarks of
670 macrophages that support productive antitumor immunity [56]. Together, these data provide
671 strong evidence that CD300e suppresses macrophage effector functions and supports the
672 establishment of a tolerogenic, immune-excluded tumor microenvironment. Our findings not only
673 reinforce the immunosuppressive nature of CD300e-expressing TAMs but also highlight CD300e as

674 a central node through which tumor-derived signals impair macrophage-mediated immune
675 surveillance. By attenuating antigen presentation even in the context of an active IFN response,
676 CD300e may serve as a critical checkpoint limiting the full activation of antitumor immunity in CRC.
677 Conditional deletion of CD300e in myeloid cells recapitulated the antitumor effects observed in full
678 knockout mice, and adoptive transfer experiments confirmed that CD300e expression on
679 macrophages alone is sufficient to drive tumor growth and suppress T-cell activation. These findings
680 firmly establish CD300e as a central regulator of macrophage-mediated immune evasion in CRC.
681 Our data position CD300e has a central modulator of monocyte-derived macrophage function in the
682 tumor microenvironment. While high macrophage infiltration has traditionally been associated with
683 favorable outcomes in CRC [19], but a growing body of evidence underscore the heterogeneity and
684 plasticity of TAMs. Notably, in CRC, high density of TAMs are now correlated with a poor prognosis
685 [23]. Our findings add functional depth to this perspective by showing that is not the number, but
686 rather the phenotype of TAMs that dictate their impact on tumor progression. In CD300e-deficient
687 tumors, despite a marked reduction in macrophage infiltration, the remaining cells were
688 functionally reprogrammed to support robust antitumor immunity. This highlights CD300e not only
689 as a marker of suppressive TAMs but also as a driver of their tumor-promoting behavior.
690 In conclusion, our study identified CD300e as a previously unrecognized orchestrator of immune
691 suppression in CRC, acting through reprogramming of TAMs. Targeting CD300e offers a promising
692 strategy to convert these cells into active effector cell in antitumor immunity. By restoring their
693 responsiveness to IFNγ and enhancing antigen presentation, CD300e blockade could enhance the
694 efficacy of immunotherapy. Future studies should focus on the development of selective CD300e
695 inhibitors and their integration into existing immunotherapy regimens, particularly in combination
696 with immune checkpoint blockade, to overcome resistance and improve outcomes for patients with
697 CRC.

Availability of Data and Material

The dataset(s) supporting the conclusions of this article is (are) available in the [repository name] repository, [unique persistent identifier and hyperlink to dataset(s) in http://format].

Author contributions

G.C. conceptually planned and supervised the study. G.C., A.B. and S.V. designed the experiments. A.B. and S.V. performed most of the experiments unless otherwise specified. G.C., A.B., S.V., L.M. S.L., M.B., S.S., M.L. and E.C. analyzed the data. S.C., S.G. and S.P. participated in the animal studies. A.B., S.V., S.G., and S.C. participated in the molecular and cellular biological experiments. S.L., M.B., and W.V. helped with the pathology-related studies. G.C., A.B., M.L., E.C. and S.S. wrote the manuscript. G.S., M.F. and W.V. participated in the clinical sample and information collection. G.S. conceptualized the clinical aspects and contributed to the clinical sample collection and data analysis. All the authors have read and approved the manuscript.

Declaration of interest

No conflicts of interest

Supporting information

Supplementary figures are included in the present version of the manuscript.

714 # References

715 1. Arnold M, Sierra MS, Laversanne M, Soerjomataram I, Jemal A, Bray F. Global patterns and
716 trends in colorectal cancer incidence and mortality. Gut. 2017;66:683–91.

717 2. Siegel RL, Giaquinto AN, Jemal A. Cancer statistics, 2024. CA A Cancer J Clinicians. 2024;74:12–
718 49.

719 3. Li J, Chen D, Shen M. Tumor Microenvironment Shapes Colorectal Cancer Progression,
720 Metastasis, and Treatment Responses. Front Med. 2022;9:869010.

721 4. Peddareddigari VG, Wang D, DuBois RN. The Tumor Microenvironment in Colorectal
722 Carcinogenesis. Cancer Microenvironment. 2010;3:149–66.

723 5. Kather JN, Halama N. Harnessing the innate immune system and local immunological
724 microenvironment to treat colorectal cancer. Br J Cancer. 2019;120:871–82.

725 6. Guo L, Wang C, Qiu X, Pu X, Chang P. Colorectal Cancer Immune Infiltrates: Significance in
726 Patient Prognosis and Immunotherapeutic Efficacy. Front Immunol. 2020;11:1052.

727 7. Pagès F, Mlecnik B, Marliot F, Bindea G, Ou F-S, Bifulco C, et al. International validation of the
728 consensus Immunoscore for the classification of colon cancer: a prognostic and accuracy study.
729 Lancet (London, England). 2018;391:2128–39.

730 8. Galon J, Pagès F, Marincola FM, Angell HK, Thurin M, Lugli A, et al. Cancer classification using
731 the Immunoscore: a worldwide task force. J Transl Med. 2012;10:205.

732 9. Hourani T, Holden JA, Li W, Lenzo JC, Hadjigol S, O'Brien-Simpson NM. Tumor Associated
733 Macrophages: Origin, Recruitment, Phenotypic Diversity, and Targeting. Front Oncol.
734 2021;11:788365.

735 10. Nasir I, McGuinness C, Poh AR, Ernst M, Darcy PK, Britt KL. Tumor macrophage functional
736 heterogeneity can inform the development of novel cancer therapies. Trends in Immunology.
737 2023;44:971–85.

738 11. Rodríguez-Morales P, Franklin RA. Macrophage phenotypes and functions: resolving
739 inflammation and restoring homeostasis. Trends in Immunology. 2023;44:986–98.

740 12. Bied M, Ho WW, Ginhoux F, Blériot C. Roles of macrophages in tumor development: a
741 spatiotemporal perspective. Cell Mol Immunol. 2023;20:983–92.

742 13. Franklin RA, Liao W, Sarkar A, Kim MV, Bivona MR, Liu K, et al. The cellular and molecular origin
743 of tumor-associated macrophages. Science. 2014;344:921–5.

744 14. Huang R, Kang T, Chen S. The role of tumor-associated macrophages in tumor immune
745 evasion. J Cancer Res Clin Oncol. 2024;150:238.

746 15. Cassetta L, Kitamura T. Macrophage targeting: opening new possibilities for cancer
747 immunotherapy. Immunology. 2018;155:285–93.

748 16. Cheng N, Bai X, Shu Y, Ahmad O, Shen P. Targeting tumor-associated macrophages as an
749 antitumor strategy. Biochemical Pharmacology. 2021;183:114354.

750 17. Zhong X, Chen B, Yang Z. The Role of Tumor-Associated Macrophages in Colorectal Carcinoma
751 Progression. Cellular physiology and biochemistry : international journal of experimental cellular
752 physiology, biochemistry, and pharmacology. 2018;45:356–65.

753 18. Kumari N, Choi SH. Tumor-associated macrophages in cancer: recent advancements in cancer
754 nanoimmunotherapies. J Exp Clin Cancer Res. 2022;41:68.

755 19. Pinto ML, Rios E, Durães C, Ribeiro R, Machado JC, Mantovani A, et al. The Two Faces of
756 Tumor-Associated Macrophages and Their Clinical Significance in Colorectal Cancer. Front
757 Immunol. 2019;10:1875.

758 20. Li Y, Chen Z, Han J, Ma X, Zheng X, Chen J. Functional and Therapeutic Significance of Tumor-
759 Associated Macrophages in Colorectal Cancer. Front Oncol. 2022;12:781233.

760 21. Gordon SR, Maute RL, Dulken BW, Hutter G, George BM, McCracken MN, et al. PD-1
761 expression by tumour-associated macrophages inhibits phagocytosis and tumour immunity.
762 Nature. 2017;545:495–9.

763 22. Zhang Y, Zhao Y, Li Q, Wang Y. Macrophages, as a Promising Strategy to Targeted Treatment
764 for Colorectal Cancer Metastasis in Tumor Immune Microenvironment. Front Immunol.
765 2021;12:685978.

766 23. Khizar H, Ali K, Wang J. From silent partners to potential therapeutic targets: macrophages in
767 colorectal cancer. Cancer Immunol Immunother. 2025;74:121.

768 24. Aguilar H, Alvarez-Errico D, García-Montero AC, Orfao A, Sayós J, López-Botet M. Molecular
769 characterization of a novel immune receptor restricted to the monocytic lineage. Journal of
770 immunology (Baltimore, Md : 1950). 2004;173:6703–11.

771 25. Isobe M, Izawa K, Sugiuchi M, Sakanishi T, Kaitani A, Takamori A, et al. The CD300e molecule in
772 mice is an immune-activating receptor. The Journal of biological chemistry. 2018;293:3793–805.

773 26. Brckalo T, Calzetti F, Pérez-Cabezas B, Borràs FE, Cassatella MA, López-Botet M. Functional
774 analysis of the CD300e receptor in human monocytes and myeloid dendritic cells. European
775 journal of immunology. 2010;40:722–32.

776 27. Pagliari M, Munari F, Toffoletto M, Lonardi S, Chemello F, Codolo G, et al. Helicobacter pylori
777 Affects the Antigen Presentation Activity of Macrophages Modulating the Expression of the
778 Immune Receptor CD300E through miR-4270. Frontiers in immunology. 2017;8:1288.

779 28. Coletta S, Salvi V, Della Bella C, Bertocco A, Lonardi S, Trevellin E, et al. The immune receptor
780 CD300e negatively regulates T cell activation by impairing the STAT1-dependent antigen
781 presentation. Sci Rep. 2020;10:16501.

782 29. Hamidzadeh K, Belew AT, El-Sayed NM, Mosser DM. The transition of M-CSF–derived human
783 macrophages to a growth-promoting phenotype. Blood Advances. 2020;4:5460–72.

784 30. Adamczyk AM, Leicaj ML, Fabiano MP, Cabrerizo G, Bannoud N, Croci DO, et al. Extracellular
785 vesicles from human plasma dampen inflammation and promote tissue repair functions in
786 macrophages. J of Extracellular Vesicle. 2023;12:12331.

787 31. Yang T, Zhang Y, Duan C, Liu H, Wang D, Liang Q, et al. CD300E+ macrophages facilitate liver
788 regeneration after splenectomy in decompensated cirrhotic patients. Exp Mol Med. 2025;57:72–
789 85.

790 32. Uhlen M, Zhang C, Lee S, Sjöstedt E, Fagerberg L, Bidkhori G, et al. A pathology atlas of the
791 human cancer transcriptome. Science. 2017;357:eaan2507.

792 33. Luo Z, Zhu J, Xu R, Wan R, He Y, Chen Y, et al. Exercise-downregulated CD300E acted as a
793 negative prognostic implication and tumor-promoted role in pan-cancer. Front Immunol.
794 2024;15:1437068.

795 34. Sato T, Stange DE, Ferrante M, Vries RGJ, Van Es JH, Van den Brink S, et al. Long-term
796 expansion of epithelial organoids from human colon, adenoma, adenocarcinoma, and Barrett's
797 epithelium. Gastroenterology. 2011;141:1762–72.

798 35. D'Elios MM, Vallese F, Capitani N, Benagiano M, Bernardini ML, Rossi M, et al. The
799 Helicobacter cinaedi antigen CAIP participates in atherosclerotic inflammation by promoting the
800 differentiation of macrophages in foam cells. Sci Rep. 2017;7:40515.

801 36. Vallese F, Mishra NM, Pagliari M, Berto P, Codolo G, De Bernard M, et al. Helicobacter pylori
802 antigenic Lpp20 is a structural homologue of Tipα and promotes epithelial-mesenchymal
803 transition. Biochimica et Biophysica Acta (BBA) - General Subjects. 2017;1861:3263–71.

804 37. Shang S, Yang C, Chen F, Xiang R, Zhang H, Dai S, et al. ID1 expressing macrophages support
805 cancer cell stemness and limit CD8+ T cell infiltration in colorectal cancer. Nat Commun.
806 2023;14:7661.

807 38. Coletta S, Lonardi S, Sensi F, D'Angelo E, Fassan M, Pucciarelli S, et al. Tumor Cells and the
808 Extracellular Matrix Dictate the Pro-Tumoral Profile of Macrophages in CRC. Cancers.
809 2021;13:5199.

810 39. Li B, Dewey CN. RSEM: accurate transcript quantification from RNA-Seq data with or without a
811 reference genome. BMC Bioinformatics. 2011;12:323.

812 40. Dunne MR, Phelan JJ, Michielsen AJ, Maguire AA, Dunne C, Martin P, et al. Characterising the
813 prognostic potential of HLA-DR during colorectal cancer development. Cancer Immunol
814 Immunother. 2020;69:1577–88.

815 41. Yu G, Wang L-G, Han Y, He Q-Y. clusterProfiler: an R Package for Comparing Biological Themes
816 Among Gene Clusters. OMICS: A Journal of Integrative Biology. 2012;16:284–7.

817 42. Wu T, Hu E, Xu S, Chen M, Guo P, Dai Z, et al. clusterProfiler 4.0: A universal enrichment tool
818 for interpreting omics data. The Innovation. 2021;2:100141.

819 43. Pelka K, Hofree M, Chen JH, Sarkizova S, Pirl JD, Jorgji V, et al. Spatially organized multicellular
820 immune hubs in human colorectal cancer. Cell. 2021;184:4734-4752.e20.

821 44. Hao Y, Stuart T, Kowalski MH, Choudhary S, Hoffman P, Hartman A, et al. Dictionary learning
822 for integrative, multimodal and scalable single-cell analysis. Nat Biotechnol. 2024;42:293–304.

823 45. Korsunsky I, Millard N, Fan J, Slowikowski K, Zhang F, Wei K, et al. Fast, sensitive and accurate
824 integration of single-cell data with Harmony. Nat Methods. 2019;16:1289–96.

825 46. Trapnell C, Cacchiarelli D, Grimsby J, Pokharel P, Li S, Morse M, et al. The dynamics and
826 regulators of cell fate decisions are revealed by pseudotemporal ordering of single cells. Nat
827 Biotechnol. 2014;32:381–6.

828 47. Korotkevich G, Sukhov V, Budin N, Shpak B, Artyomov MN, Sergushichev A. Fast gene set
829 enrichment analysis [Internet]. Bioinformatics; 2016 [cited 2025 Jun 17]. Available from:
830 http://biorxiv.org/lookup/doi/10.1101/060012

831 48. Subramanian A, Tamayo P, Mootha VK, Mukherjee S, Ebert BL, Gillette MA, et al. Gene set
832 enrichment analysis: A knowledge-based approach for interpreting genome-wide expression
833 profiles. Proc Natl Acad Sci USA. 2005;102:15545–50.

834 49. Castanza AS, Recla JM, Eby D, Thorvaldsdóttir H, Bult CJ, Mesirov JP. Extending support for
835 mouse data in the Molecular Signatures Database (MSigDB). Nat Methods. 2023;20:1619–20.

836 50. Lavender N, Yang J, Chen S-C, Sai J, Johnson CA, Owens P, et al. The Yin/Yan of CCL2: a minor
837 role in neutrophil anti-tumor activity in vitro but a major role on the outgrowth of metastatic
838 breast cancer lesions in the lung in vivo. BMC Cancer. 2017;17:88.

839 51. Molgora M, Esaulova E, Vermi W, Hou J, Chen Y, Luo J, et al. TREM2 Modulation Remodels the
840 Tumor Myeloid Landscape Enhancing Anti-PD-1 Immunotherapy. Cell. 2020;182:886-900.e17.

841 52. Parang B, Barrett CW, Williams CS. AOM/DSS Model of Colitis-Associated Cancer. In: Ivanov AI,
842 editor. Gastrointestinal Physiology and Diseases [Internet]. New York, NY: Springer New York;
843 2016 [cited 2024 Aug 30]. p. 297–307. Available from: http://link.springer.com/10.1007/978-1-
844 4939-3603-8_26

845 53. Wang S, Wang J, Chen Z, Luo J, Guo W, Sun L, et al. Targeting M2-like tumor-associated
846 macrophages is a potential therapeutic approach to overcome antitumor drug resistance. npj
847 Precis Onc. 2024;8:31.

848 54. Rashidian M, LaFleur MW, Verschoor VL, Dongre A, Zhang Y, Nguyen TH, et al. Immuno-PET
849 identifies the myeloid compartment as a key contributor to the outcome of the antitumor
850 response under PD-1 blockade. Proc Natl Acad Sci USA. 2019;116:16971–80.

851 55. Su P, Wang Q, Bi E, Ma X, Liu L, Yang M, et al. Enhanced Lipid Accumulation and Metabolism
852 Are Required for the Differentiation and Activation of Tumor-Associated Macrophages. Cancer
853 Research. 2020;80:1438–50.

854 56. Lecoultre M, Dutoit V, Walker PR. Phagocytic function of tumor-associated macrophages as a
855 key determinant of tumor progression control: a review. J Immunother Cancer. 2020;8:e001408.

856

		CRC patients (n=8)
Age	Median (range), years	74 (65-84)
Sex	Male Female	6 (75%) 2 (25%)
Grade	1 2 3 4	0 5 (62.5%) 3 (37.5%) 0
TNM	I II III IV	0 4 (50%) 4 (50%) 0
Tumor histotype	Adenocarcinoma	8 (100%)

857 **Table 1. Clinicopathological characteristics of CRC patients.** CRC: colorectal cancer; TNM: pathological tumor, node,
858 metastasis stage.
859
860
861
862
863
864
865
866
867
868
869
870
871
872
873
874
875

Antigen	Fluorophore	Clone
Human monocytes/macrophages panel		
CD206	BB515	19.2
CD300e	PE	UPH2
CD86	PE-Cy7	IT2.2
MHC-II	APC	L243
Fixable viability dye (L/D)	eFluor780	
Mouse blood and bone marrow panel		
CD11b	BV421	M1/70
Fixable viability dye (L/D)	Zombie Aqua™	
NK-1.1	BV605	PK136
Ly6C	BV785	HK1.4
CD45	FITC	30-F11
CD19	PE	1D3/CD19
CD8a	PerCP-Cy5.5	53-6.7
Ly6G	PE-Cy7	1A8
CD4	APC	GK1.5
CD3e	APC-Cy7	145-2C11
Mouse myeloid panel		
Ly6C	BV421	HK1.4
CD3	BV510	145-2C11
CD19	BV510	6D5
NK-1.1	BV510	PK136
CD11b	BV785	M1/70
I-A/I-E	PE/Dazzle	M5/114.15.2
H-2Kb/H-2Db	PerCP/Cy5.5	28-8-6
F4/80	PE-Cy7	BM8
Ly6G	AlexaFluor700	1 A8
Fixable viability dye (L/D)	eFluor780	
Mouse lymphoid panel		
Fixable viability dye	Zombie Aqua™	
CD69	BV605	H1.2F3
CD4	BV650	RM4-5
CD11b	BV785	M1/70
CD62L	FITC	MEL-14
CD8a	AlexaFluor700	QA17AO7
CD3e	APC-Cy7	145-2C11
Mouse T cells panel		
Fixable viability dye (L/D)	Zombie Aqua™	
CD4	BV650	RM4-5
IFN-γ	FITC	XMG1.2
CD19	PE	1D3/CD19
CD8a	PerCP-Cy5.5	53-6.7
CD3	APC	145-2C11

876 **Table 2:** Detailed list of antibody panels used for flow cytometry analysis.

877 ## Figure legends

878 **Figure 1: CD300e is expressed by tumor-infiltrating macrophages in colorectal cancer and is**
879 **associated with the immunosuppressive profile.**

880 A) CD300e expression by western blot and qPCR in CRC tissue vs matched normal mucosa (mean ±
881 SD of 8 CRC patients). *p value ≤0.05.

882 B) qRT–PCR expression of MHC-II, CIITA and STAT1 (mean ± SD of 6 CRC patients). ***p value ≤0.001;
883 ****p value ≤0.0001.

884 C) IHC staining of macrophages (CD163^{+} blue) expressing CD300e (brown) and MHC-II (red); arrows
885 highlight CD300e^{+}/MHC-II^{low} macrophages. The histogram shows the percentage of CD300e^{+}/MHC-
886 II^{low} macrophages expressed as the mean ± SD of 8 CRC patients. Statistical significance was
887 determined by Student's t test. CRC = colorectal cancer; NM = normal colonic mucosa. *p value
888 ≤0.05.

889 D) UMAP plot showing the transcriptional states of myeloid cells infiltrating colorectal cancer
890 samples identified via scRNA-seq.

891 E) Bar plot showing the contribution of each cluster identified via scRNA-seq divided by the origin
892 of the sample. T, tumoral sample; N, tumor adjacent sample.

893 F) Violin plot showing the normalized expression levels of CD300E across the clusters identified via
894 scRNA-seq divided by the origin of the samples. Adjusted p value from the "Seurat" DESeq2 test.
895 *** adjusted p value < 0.001.

896 **Figure 2. Tumor-derived colon organoids induce CD300e expression and immunosuppressive**
897 **programming in human monocytes-derived macrophages.**

898 A) Scheme of the experimental set up. Image created with Biorender. NCO = normal colon organoid;
899 TCO = tumor colon organoid. Created with Biorender.

900 B) CD68 expression analysis by flow cytometry of monocytes at time 0 (dotted line) and monocytes-
901 derived macrophages (MDM) cocultured for 5 d with NCO or TCO (n = 4 different monocyte donors
902 cocultured with 4 NCO lines and 4 TCO lines). Data are expressed as Median Fluorescence Intensity
903 (MFI). *p value ≤0.05.

904 C) Flow cytometry and qRT-PCR of CD300e on MDMs cocultured for 5 d with NCO or TCO (n = 4
905 different monocyte donors cocultured with 4 NCO and 4 TCO lines). **p value ≤0.01.

906 D) Flow cytometry analysis of MDMs (MHC-II, CD86, MHC-I, CD206) after 5 d of coculture. *p value
907 ≤0.05; **p value ≤0.01.

908 E) Quantification of IL-6 and IL-10 released in coculture supernatants by ELISA assay. **p value
909 ≤0.01.

910 **Figure 3. CD300e$^{-/-}$ mice develop a lower tumor burden in the AOM/DSS CRC model.**

911 A) Kaplan–Meier survival analysis.

912 B) Weights of the mice throughout the AOM/DSS (n = 20 CD300e$^{+/+}$ and 20 CD300e$^{-/-}$ mice).
913 Statistical significance was determined by two-way ANOVA and Šídák's multiple comparisons test:
914 **p value ≤0.01.

915 C) Colon images and colon length measurements after AOM/DSS treatment (n = 20 CD300e$^{+/+}$ and
916 20 CD300e$^{-/-}$ mice; scale bar = 1 cm). ***p value ≤0.001.

917 D) Images of longitudinally opened colons from CD300e$^{+/+}$ and CD300e$^{-/-}$ mice (scale bar = 1 cm).
918 Number of tumors/mouse (left) and tumor area/mouse (right) (n = 20 CD300e$^{+/+}$ and 20 CD300e$^{-/-}$
919 mice; scale bar = 1 cm). Arrowheads indicate adenomas. *p value ≤0.05; **p value ≤0.01.

920 E) UMAPs showing the transcriptional states of adenoma-infiltrating myeloid cells On the right, the
921 bar plot shows the contribution of each cluster identified via scRNA-seq divided by the origin of
922 the samples: CD300e$^{+/+}$ and CD300e$^{-/-}$ mice.

923 F) Lolly plot showing the normalized enrichment scores of the GSEA of hallmarks between
924 CD300e-/- and CD300e$^{+/+}$.

925 G) Heatmap of the z score of the gene of interest derived from the significant pathway from the
926 GSEA.

927 H) IFN-γ production by mesenteric CD4^{+} and CD8^{+} T cells. **p value ≤0.01.

928 **Figure 4. CD300e conditional knockout (CD300e$^{fl/fl}$LysM^{Cre}) mice develop a lower tumor burden.**

929 A) Weights of the mice throughout the AOM/DSS (n = 4 CD300e$^{fl/fl}$ and 4 CD300e^{LysM} mice). Statistical
930 significance was determined by two-way ANOVA and Šídák's multiple comparisons test: ****p value
931 ≤0.0001.

932 B) Colon images and colon length measurements after AOM/DSS treatment (scale bar = 1 cm).
933 Arrowheads indicate adenomas.

934 C) Images of longitudinally opened colons from CD300e$^{+/+}$ and CD300e$^{-/-}$ mice (left; scale bar = 1 cm).
935 Number of tumors/mouse (middle) and tumor area/mouse (right). Statistical significance was
936 determined by Student's t test. **p value ≤0.01.

937 D) IFN-γ production by mesenteric CD4^{+} and CD8^{+} T cells. *p value ≤0.05.

938 **Figure 5. CD300e ablation delays MC38 tumor growth and modifies the tumor-immune infiltrate.**

939 A) Growth kinetics of MC38 colon adenocarcinoma in mice (mean ± SD of n = 13 CD300e$^{+/+}$ and 13
940 CD300e$^{-/-}$ mice). Statistical significance was determined by two-way ANOVA and Šídák's multiple
941 comparisons test: * p value ≤0.05; **** p value ≤0.0001.

942 B) Images of tumors (left), tumor weights (middle) and final tumor volumes (right). ** p value ≤0.01.

943 C) Myeloid cells were identified as CD45^{+}CD11b^{+} and neutrophils were identified as
944 CD45^{+}CD11b^{+}Ly6G^{+}Ly6C^{+} and are presented as a percentage of CD45^{+} cells (n = 10 CD300e$^{+/+}$ and 10
945 CD300e$^{-/-}$ mice). * p value ≤0.05.

946 D) Ly6G^{-}Ly6C^{+} monocytes gated on CD45^{+}CD11b^{+} cells are shown as a percentage of CD45$^{+\ cells}$. *p
947 value ≤0.05.

948 E) MHC-II- and MHC-I-expressing tumor-infiltrated monocytes gated on CD45^{+}CD11b^{+}Ly6G^{-}Ly6C^{+}
949 cells are shown as percentages of Ly6G^{-}Ly6C$^{+\ cells}$. *p value ≤0.05; **p value ≤0.01.

950 F) F4/80^{+} macrophages gated on CD45^{+}CD11b^{+}Ly6C^{-} cells are shown as a percentage of CD45$^{+\ cells}$.
951 *p value ≤0.05.

952 G) MHC-II- and MHC-I-expressing tumor-infiltrated macrophages gated on CD45^{+}CD11b^{+}Ly6C^{-}
953 F4/80+ cells are shown as percentages of F4/80^{+} cells. *p value ≤0.05; ****p value ≤0.0001.

954 H) CD4^{+} and CD8^{+} T lymphocyte populations in tumors gated on CD45^{+}CD3^{+} cells are shown as
955 percentages of CD45^{+} cells (means ± SDs of 8 CD300e$^{+/+}$ and 8 CD300e$^{-/-}$ mice). *p value ≤0.05.

956 I) Early active CD4^{+} and CD8^{+} T cells were identified as CD69^{+} cells and are presented as the
957 percentage of CD3^{+} cells (mean ± SD of 5 CD300e$^{+/+}$ and 5 CD300e$^{-/-}$ mice). **p value ≤0.01.

958 J) Effector memory $CD4^+$ and $CD8^+$ T cells were identified as $CD44^+CD62L^-$ cells and are presented as
959 percentages of $CD3^{+\ cells}$. *p value ≤0.05.

960 K) IFN-γ production by tumor-infiltrating $CD4^+$ and $CD8^+$ T cells is shown as the percentage of $CD3^+$
961 cells (mean ± SD of 8 $CD300e^{+/+}$ and 8 $CD300e^{-/-}$ mice). **p value ≤0.01.

962 L) GZMB and perforin expression by tumor-infiltrating $CD8^+$ T lymphocytes is shown as the
963 percentage of $CD3^+$ cells (mean ± SD of 10 $CD300e^{+/+}$ and 10 $CD300e^{-/-}$ mice). *p value ≤0.05.

964 **Figure 6: CD300e deficiency improves phagocytic capacity and T-cell proliferation.**

965 A) Representative images of the phagocytosis assay of F4/80+ macrophages isolated from $CD300e^{+/+}$
966 and $CD300e^{-/-}$ tumors incubated with Zymosan A BioParticles™. Nuclei were stained with DAPI
967 (blue), F4/80 was used as a macrophage marker (green), and Zymosan BioParticles™ are visualized
968 in red (left). Scale bar = 50 µm. The percentage of phagocytic macrophages (middle) was calculated
969 as the number of phagocytic macrophages (macrophages that internalized ≥1 bioparticle) among
970 the total number of macrophages; ten randomly acquired images per sample were analyzed (n=3
971 $CD300e^{+/+}$ and 3 $CD300e^{-/-}$ mice; right panel). The phagocytic index (right) was calculated as the
972 percentage of phagocytic macros × the mean number of fluorescent beads per macrophage. *p
973 value ≤0.05.

974 B) Proliferation index of T cells as measured by CellTrace™ Violet dilution after 4 d of activation in
975 vitro with anti-CD3 and anti-CD28 antibodies in the presence of allogenic tumor-isolated $F4/80^+$ cells
976 from $CD300e^{+/+}$ and $CD300e^{-/-}$ mice at a 1:3 ratio. *p value ≤0.05.

977 **Figure 7: Tumor-infiltrating macrophages lacking CD300e expression are responsible for**
978 **modulating the tumor microenvironment in $CD300e^{+/+}$ mice.**

979 A) Schematic representation of the experimental workflow. Created with Biorender.

980 B) Growth kinetics of tumors in CD300e$^{+/+}$ mice (mean ± SD of n = 5 CD300e$^{+/+}$ macrophages and 5
981 CD300e$^{-/-}$ macrophages). Statistical significance was determined by two-way ANOVA and Šídák's
982 multiple comparisons test: *p value ≤0.05; **p value ≤0.01; **** p value ≤0.0001.

983 C) Images of tumors (left), tumor weights (middle) and final tumor volumes (right). *p value ≤0.05;
984 **p value ≤0.01.

985 D) IFN-γ production by tumor-infiltrating CD4^{+} and CD8^{+} T cells is expressed as an n-fold difference
986 between CD300e$^{+/+}$ mice injected with CD300e$^{-/-}$ macrophages and CD300e$^{+/+}$ mice injected with
987 CD300e$^{+/+}$ macrophages. *p value ≤0.05.

988 E) GZMB and perforin production by tumor-infiltrating CD8^{+} T lymphocytes expressed as *n*-fold of
989 CD300e$^{+/+}$ mice injected with CD300e$^{-/-}$ macrophages vs CD300e$^{+/+}$ mice injected with CD300e$^{+/+}$
990 macrophages. *p value ≤0.05.

991

Figure 1

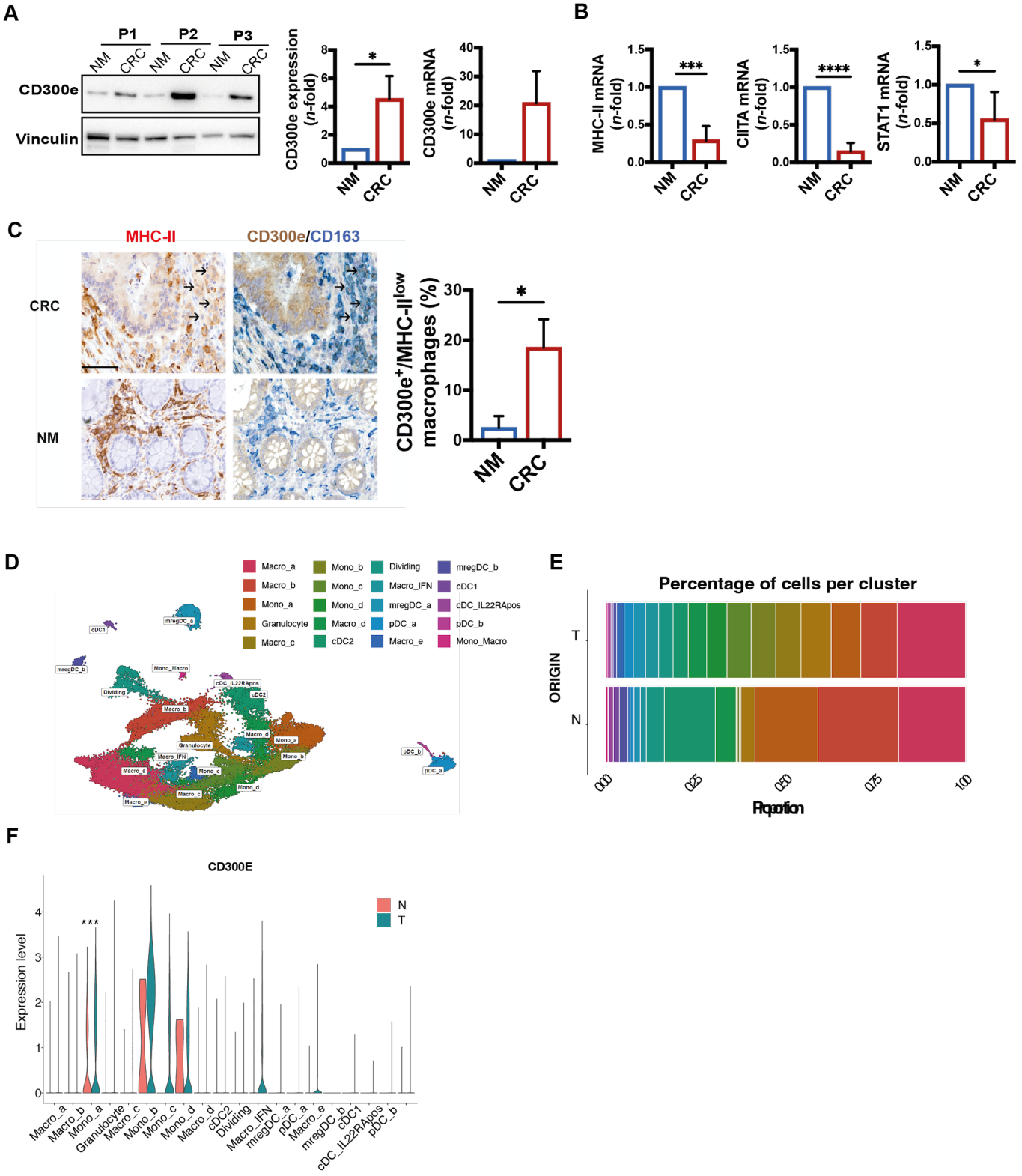
A
P1
P2
P3
NM
CRC
CD300e
Vinculin
CD300e expression (n-fold)
CD300e mRNA (n-fold)
B
MHC-II mRNA (n-fold)
CIITA mRNA (n-fold)
STAT1 mRNA (n-fold)
C
MHC-II
CD300e/CD163
CRC
NM
CD300e+/MHC-IIlow macrophages (%)
D
Macro_a
Macro_b
Mono_a
Granulocyte
Macro_c
Mono_b
Mono_c
Mono_d
Macro_d
cDC2
Dividing
Macro_IFN
mregDC_a
pDC_a
Macro_e
mregDC_b
cDC1
cDC_IL22RApos
pDC_b
Mono_Macro
E
Percentage of cells per cluster
ORIGIN
T
N
Proportion
F
CD300E
Expression level
N
T

Figure 2

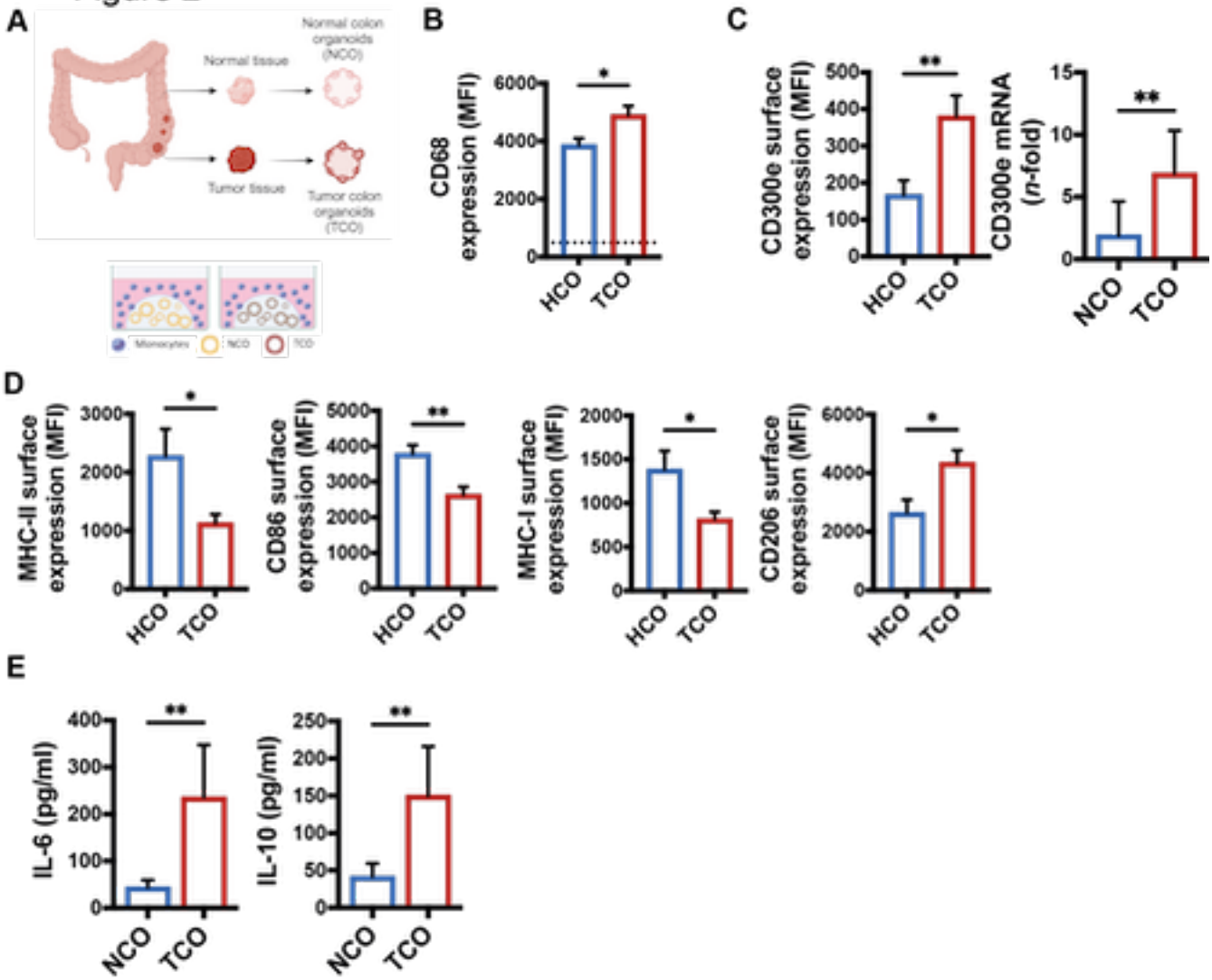
A
Normal colon organoids (NCO)
Normal tissue
Tumor tissue
Tumor colon organoids (TCO)
Monocytes
NCO
TCO
B
CD68 expression (MFI)
6000
4000
2000
0
*
HCO
TCO
C
CD300e surface expression (MFI)
500
400
300
200
100
0
**
HCO
TCO
CD300e mRNA (n-fold)
15
10
5
0
**
NCO
TCO
D
MHC-II surface expression (MFI)
3000
2000
1000
0
*
HCO
TCO
CD86 surface expression (MFI)
5000
4000
3000
2000
1000
0
**
HCO
TCO
MHC-I surface expression (MFI)
2000
1500
1000
500
0
*
HCO
TCO
CD206 surface expression (MFI)
6000
4000
2000
0
*
HCO
TCO
E
IL-6 (pg/ml)
400
300
200
100
0
**
NCO
TCO
IL-10 (pg/ml)
250
200
150
100
50
0
**
NCO
TCO

Figure 3

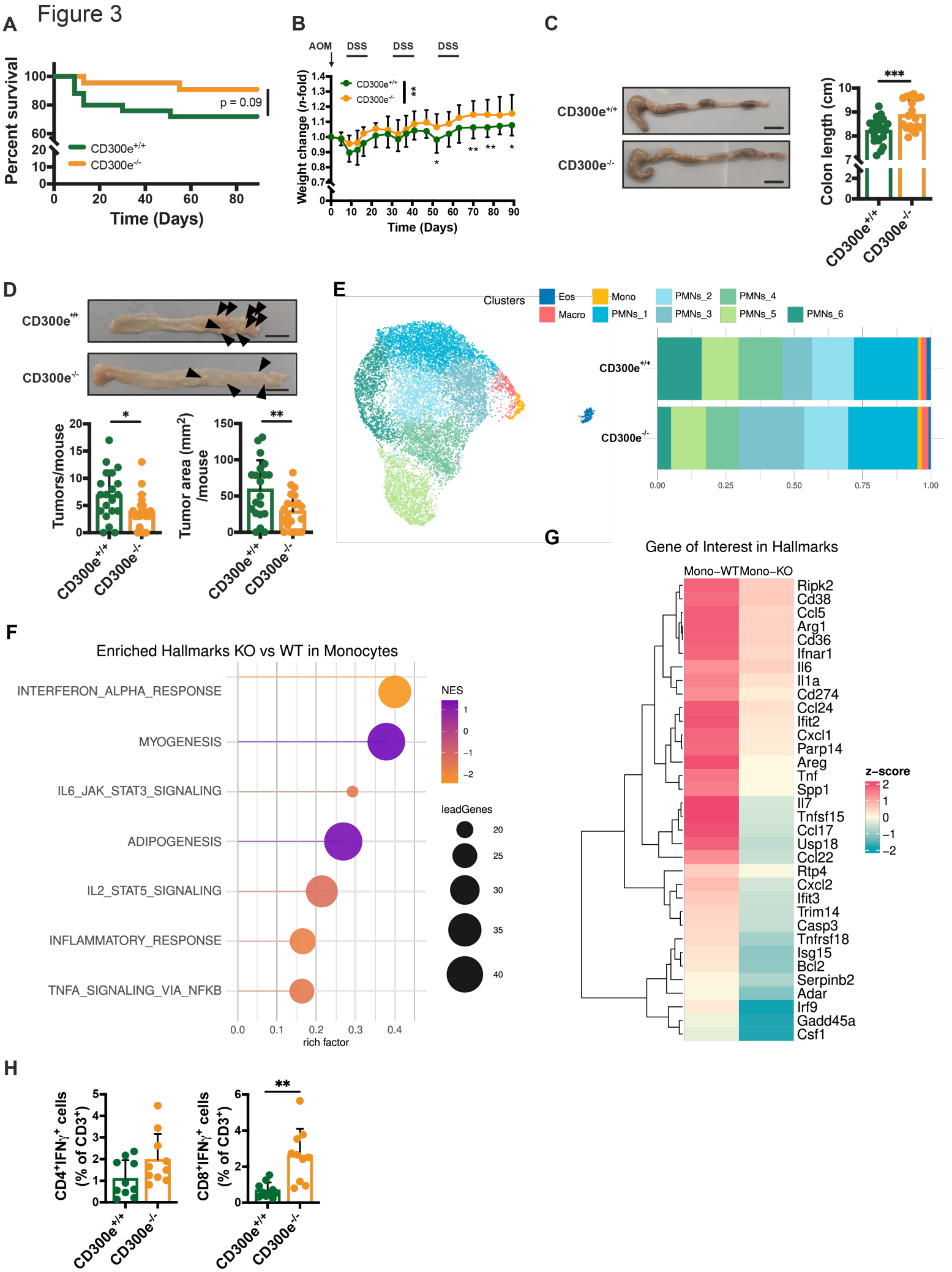
A
Percent survival
Time (Days)
p = 0.09
CD300e+/+
CD300e-/-
B
AOM
DSS
DSS
DSS
Weight change (n-fold)
Time (Days)
C
CD300e+/+
CD300e-/-
Colon length (cm)
***
D
CD300e+/+
CD300e-/-
Tumors/mouse
Tumor area (mm2) /mouse
E
Clusters
Eos
Mono
PMNs_2
PMNs_4
Macro
PMNs_1
PMNs_3
PMNs_5
PMNs_6
G
Gene of Interest in Hallmarks
Mono−WT
Mono−KO
Ripk2
Cd38
Ccl5
Arg1
Cd36
Ifnar1
Il6
Il1a
Cd274
Ccl24
Ifit2
Cxcl1
Parp14
Areg
Tnf
Spp1
Il7
Tnfsf15
Ccl17
Usp18
Ccl22
Rtp4
Cxcl2
Ifit3
Trim14
Casp3
Tnfrsf18
Isg15
Bcl2
Serpinb2
Adar
Irf9
Gadd45a
Csf1
z−score
F
Enriched Hallmarks KO vs WT in Monocytes
INTERFERON_ALPHA_RESPONSE
MYOGENESIS
IL6_JAK_STAT3_SIGNALING
ADIPOGENESIS
IL2_STAT5_SIGNALING
INFLAMMATORY_RESPONSE
TNFA_SIGNALING_VIA_NFKB
NES
leadGenes
rich factor
H
CD4+IFNγ+ cells (% of CD3+)
CD8+IFNγ+ cells (% of CD3+)

Figure 4

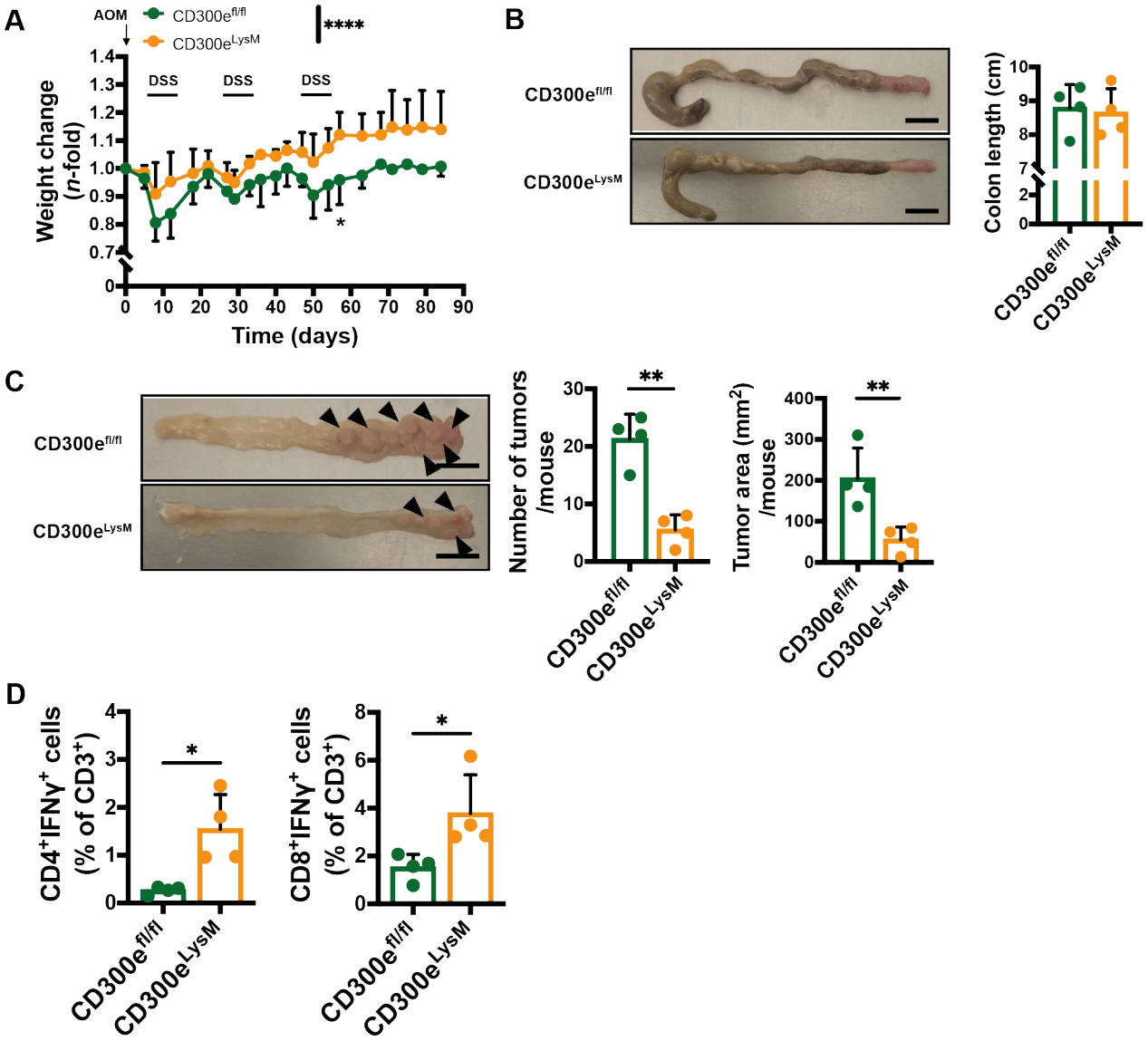
A
AOM
CD300e^fl/fl
CD300e^LysM
****
DSS
DSS
DSS
Weight change (n-fold)
Time (days)
B
CD300e^fl/fl
CD300e^LysM
Colon length (cm)
C
CD300e^fl/fl
CD300e^LysM
Number of tumors /mouse
Tumor area (mm^2) /mouse
D
CD4^+IFNγ^+ cells (% of CD3^+)
CD8^+IFNγ^+ cells (% of CD3^+)

Figure 5

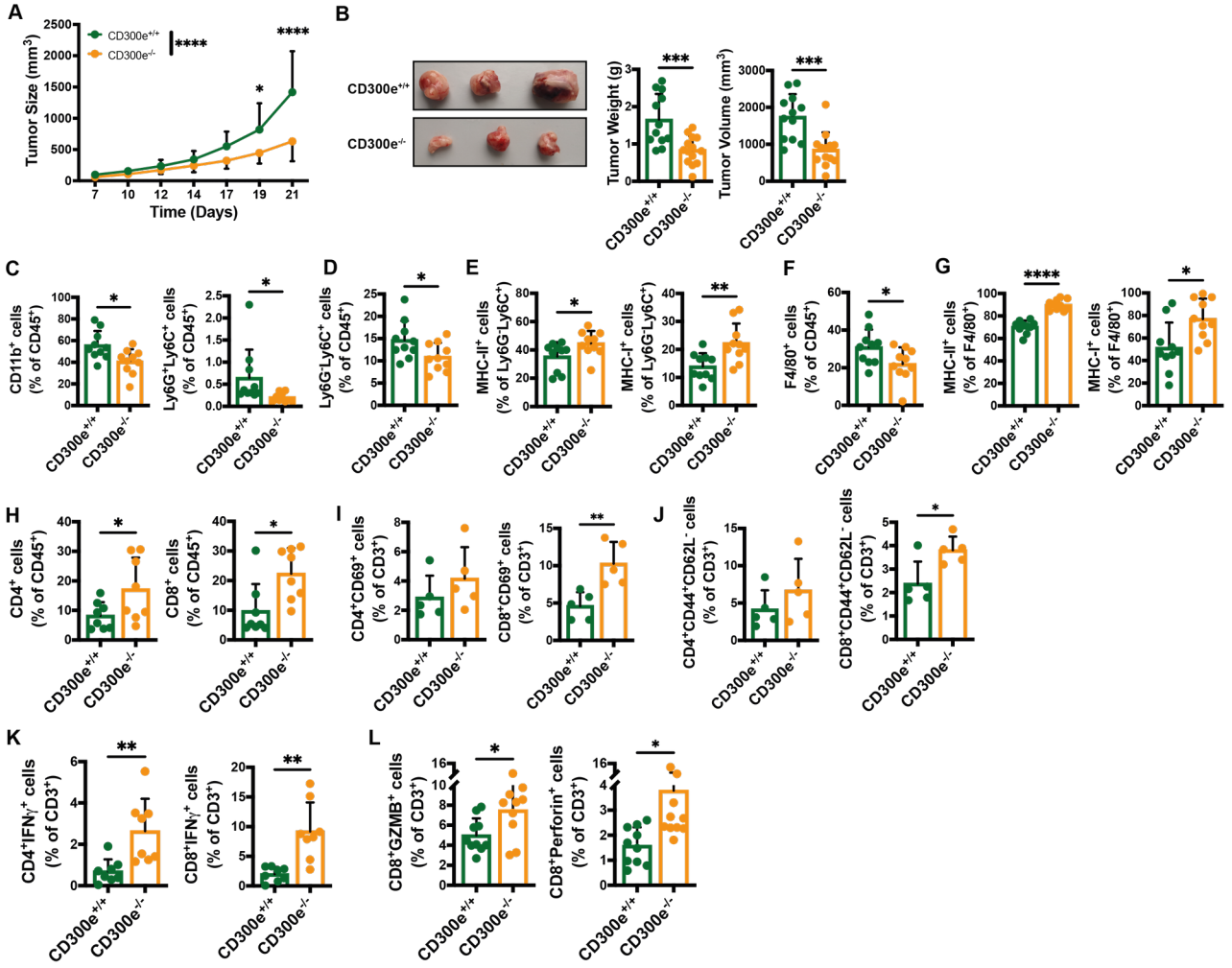
A
Tumor Size (mm³)
CD300e+/+
CD300e-/-
****
*
****
Time (Days)
B
CD300e+/+
CD300e-/-
Tumor Weight (g)
***
Tumor Volume (mm³)
***
C
CD11b+ cells (% of CD45+)
Ly6G+Ly6C+ cells (% of CD45+)
D
Ly6G-Ly6C+ cells (% of CD45+)
E
MHC-II+ cells (% of Ly6G-Ly6C+)
MHC-I+ cells (% of Ly6G-Ly6C+)
F
F4/80+ cells (% of CD45+)
G
MHC-II+ cells (% of F4/80+)
MHC-I+ cells (% of F4/80+)
H
CD4+ cells (% of CD45+)
CD8+ cells (% of CD45+)
I
CD4+CD69+ cells (% of CD3+)
CD8+CD69+ cells (% of CD3+)
J
CD4+CD44+CD62L- cells (% of CD3+)
CD8+CD44+CD62L- cells (% of CD3+)
K
CD4+IFNγ+ cells (% of CD3+)
CD8+IFNγ+ cells (% of CD3+)
L
CD8+GZMB+ cells (% of CD3+)
CD8+Perforin+ cells (% of CD3+)

Figure 6

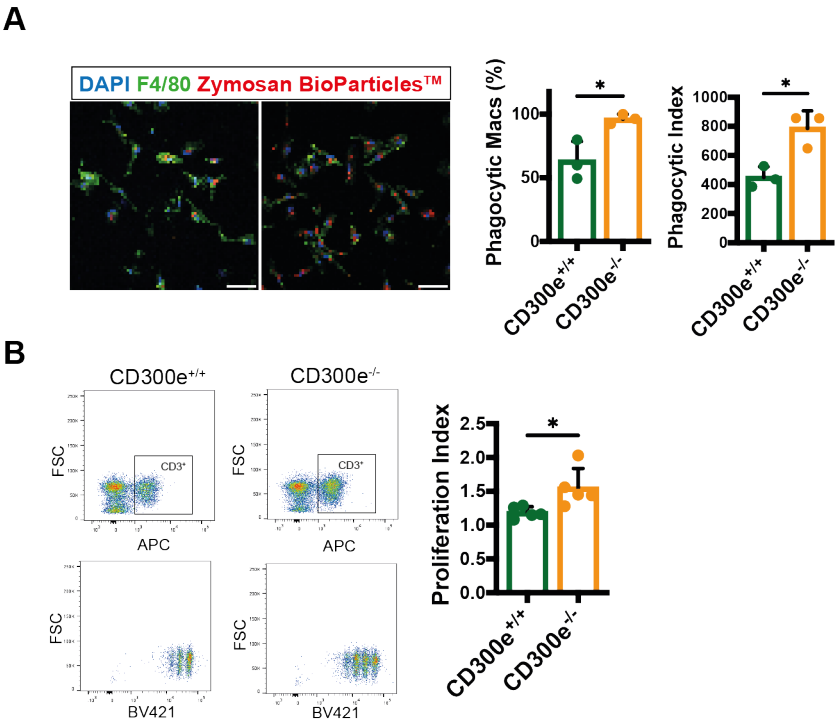
A
DAPI F4/80 Zymosan BioParticles™
Phagocytic Macs (%)
100
50
0
*
CD300e+/+
CD300e-/-
Phagocytic Index
1000
800
600
400
200
0
*
CD300e+/+
CD300e-/-
B
CD300e+/+
CD300e-/-
FSC
CD3+
APC
FSC
CD3+
APC
FSC
BV421
FSC
BV421
Proliferation Index
2.5
2.0
1.5
1.0
0.5
0.0
*
CD300e+/+
CD300e-/-

Figure 7

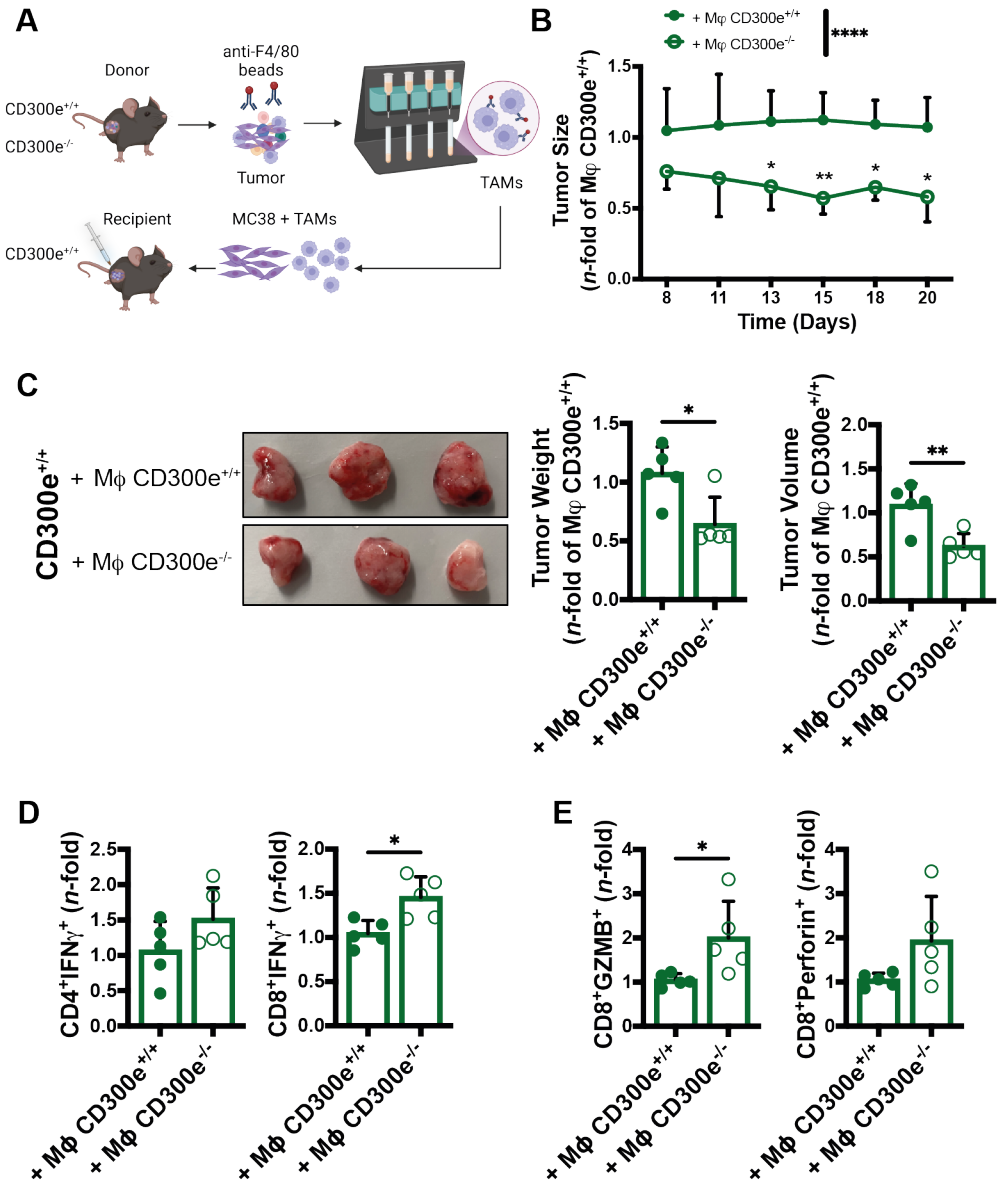
A
Donor
CD300e+/+
CD300e-/-
anti-F4/80 beads
Tumor
TAMs
Recipient
CD300e+/+
MC38 + TAMs
B
+ Mφ CD300e+/+
+ Mφ CD300e-/-
****
Tumor Size (n-fold of Mφ CD300e+/+)
Time (Days)
C
CD300e+/+
+ Mϕ CD300e+/+
+ Mϕ CD300e-/-
Tumor Weight (n-fold of Mφ CD300e+/+)
Tumor Volume (n-fold of Mφ CD300e+/+)
+ Mϕ CD300e+/+
+ Mϕ CD300e-/-
D
CD4+IFNγ+ (n-fold)
CD8+IFNγ+ (n-fold)
E
CD8+GZMB+ (n-fold)
CD8+Perforin+ (n-fold)